nature energy

Article

https://doi.org/10.1038/s41560-026-01981-3

Dry electrode architecture design to push energy density limits at the cell level

Received: 29 July 2025

Accepted: 15 January 2026

Published online: 18 February 2026

Check for updates

Minghao Zhang[1], Boyan K. Stoychev[2], Xingyu Zhang[3,4], Weiliang Yao[1], Shen Wang[5], Mehdi Chouchane[1], Na Ri Park[5], Chen-Jui Huang[1], Rishika Jakhar[1], Ganesh Raghavendran[5], Naohiro Tojima[5], Tingting Yang[6], Haifeng Gao[6], Zhao Liu[6], Alejandro A. Franco[3,4,7,8] ✉, Oleg G. Shpyrko[2] ✉ & Ying Shirley Meng[1] ✉

High-energy lithium batteries require electrode architectures that enable high areal capacity, high active material content, and stable high-voltage operation—requirements that conventional slurry-based electrodes struggle to meet due to inefficient electron percolation, parasitic reactions, and limited processing-architecture predictability. Here we design and validate a dry-processed electrode architecture that leverages molecular-level coupling between fibrous carbon and binder to promote efficient electronic conduction while suppressing high-voltage interfacial degradation. This architecture achieves areal loadings >5 mAh cm^{-2} with >99 wt% active material and supports stable operation up to 4.70 V without compromising rate capability. The 4.55 V NMC811||graphite pouch cells retain 78% capacity after 1,000 cycles at C/3-rate, with average Coulombic efficiency exceeding 99.9%. These results are achieved without material-level modifications or specialized electrolyte additives, highlighting the potential of electrode engineering alone to unlock the intrinsic performance of active materials even under demanding conditions of high areal loading and maximum active material content.

Maximizing the energy density of lithium batteries is a central challenge in advancing next-generation energy storage systems for electric vehicles and grid applications[1]. Achieving this requires electrode architectures that not only deliver high areal capacities but also maximize the proportion of electrochemically active components. Increasing areal capacity substantially boosts energy density at lower loadings, yet gains diminish beyond ~5–6 mAh cm^{-2} due to the disproportionate contribution of inactive materials (carbon and binder) to total cell mass. By contrast, increasing the active material weight ratio shows a linear relationship with energy density, as even small reductions in binder and conductive additive content directly improve the efficiency of cell mass utilization. Enhancing the active material ratio, particularly beyond the industry-standard values of ~95–96 wt%, can therefore yield substantial energy density increase. In addition to improving gravimetric energy density, reducing low-density components such as carbon and binder also leads to a measurable increase in volumetric energy density, which is critical for space-constrained applications[2]. Although areal loading and active material ratio are often treated independently[3], they must be co-optimized to unlock the full potential of lithium batteries.

[1]Pritzker School of Molecular Engineering, The University of Chicago, Chicago, IL, USA. [2]Department of Physics, University of California San Diego, La Jolla, CA, USA. [3]Laboratoire de Réactivité et de Chimie des Solides, Université de Picardie Jules Verne, Hub de l'Energie, UMR CNRS 7314, Amiens Cedex, France. [4]Reseau sur le Stockage Electrochimique de l´Energie, FR CNRS 3459, Hub de l'Energie, UMR CNRS 7314, Amiens Cedex, France. [5]Department of NanoEngineering, University of California San Diego, La Jolla, CA, USA. [6]Thermo Fisher Scientific, Hillsboro, OR, USA. [7]ALISTORE-European Research Institute, FR CNRS 3104, Hub de l'Energie, UMR CNRS 7314, Amiens Cedex, France. [8]Institut Universitaire de France, Paris Cedex, France. ✉e-mail: alejandro.franco@u-picardie.fr; oshpyrko@ucsd.edu; shirleymeng@uchicago.edu

Despite efforts to optimize electrode architecture, a substantial gap remains between the theoretical and practical capacity of many state-of-the-art cathode materials, particularly high-Ni layered oxides such as $LiNi_{0.8}Mn_{0.1}Co_{0.1}O_2$ (NMC811)[4]. Although their theoretical capacity exceeds 270 mAh g^{-1}, conventional voltage-limited cycling protocols typically access only ~70% of this value[5]. These voltage cutoffs are imposed to mitigate structural degradation and transition-metal dissolution, both triggered by parasitic reactions at the cathode–electrolyte interphase (CEI)[6]. In particular, operating high-Ni NMCs (NMC stands for Ni, Mn and Co) above 4.30 V induces electrolyte decomposition and surface reconstruction, leading to interfacial instabilities that compromise long-term cyclability[7,8]. As a result, much of the electrochemically active material remains untapped, limiting commercial lithium-ion batteries' cell-level energy density.

Supplementary Table 1 presents that cycling of high-Ni NMC cathodes with graphite anodes at voltage cutoffs above 4.40 V has been explored to increase energy density. Most approaches focus on materials-level modifications, including electrolyte reformulations[9,10], surface coatings on NMC particles[11] and bulk structural doping[12], aiming to mitigate high-voltage degradation. Although these strategies offer incremental improvements, cycling stability remains limited, with capacity fading within 300–500 cycles[13,14]. These results highlight the persistent challenges of sustaining long-term performance at high voltages. Overcoming this voltage-induced capacity ceiling requires not only stable materials but also electrode architectures and interfacial designs that suppress high-voltage degradation while maintaining efficient electronic and ionic transport across thick electrodes.

In addition to voltage stability challenges, Supplementary Table 1 also presents key limitations in electrode engineering using conventional slurry-casting methods. Although some studies report cathodes with areal loadings exceeding 15 mg cm^{-2} or 3 mAh cm^{-2} (ref. 14), these often rely on high contents of inactive components, resulting in active material weight ratios around 90 wt%. By contrast, electrodes achieving higher active material ratios (>95 wt%) tend to be restricted to much lower areal loadings, typically below 10 mg cm^{-2} (ref. 15), due to poor mechanical integrity, high likelihood of delamination at the current collector interface, and challenges in maintaining electronic percolation network during the drying process[16]. These limitations become particularly critical at elevated cutoff voltages, where increased electrochemical and structural stresses throughout the electrode exacerbate parasitic reactions and mechanical failure[17].

Unlike slurry casting, dry processing mechanically integrates active material, conductive carbon and binder without liquid-phase transport, enabling structurally coherent electrodes with minimal inactive content[18]. Although dry electrode processing offers clear manufacturing advantages, including reduced production time and energy consumption[19], how processing conditions govern electrode architecture remains poorly understood[20,21], limiting its full potential to achieve thick, high-voltage cathodes with ultrahigh active material content.

In this work, we employ operando single-particle X-ray diffraction (XRD) to observe phase transformation dynamics and structural heterogeneity in high-loading NMC811 cathodes during cycling above 4.40 V. This approach enables us to track the evolution of lattice, strain and phase heterogeneity in real time—phenomena that are otherwise obscured in bulk-averaged diagnostics[22,23]. The insights gained from these operando studies reveal the mechanistic origins of failure in conventional slurry-processed electrodes and motivate the rational design of a dry-processed electrode architecture that addresses these issues with both high areal loadings (>5 mAh cm^{-2}) and higher active material ratios (>99 wt%). We further integrate coarse-grained molecular dynamics (CGMD) simulations[24] to elucidate mesoscale interactions between polytetrafluoroethylene (PTFE) binder and functionalized vapour-grown carbon fibre (VGCF) under dry mixing, revealing how shear and compaction govern conductive network formation and interfacial coupling. These insights establish quantitative structure–processing–function relationships essential for the rational design of dry-processed thick electrodes that enables 4.55 V NMC811||graphite pouch cells.

Results and discussion

Reaction heterogeneity in thick electrode at high voltage

Thick electrodes introduce pronounced heterogeneities in ionic and electronic transport, which lead to non-uniform state-of-charge distributions across the electrode thickness[17]. This inhomogeneity induces localized overpotentials that scale with the logarithmic dependence of reaction rate, governed by Butler–Volmer behaviour. To probe the spatial and temporal reaction heterogeneity in high-loading cathodes under elevated voltage conditions, we employed operando single-particle XRD, which enables direct correlation between structural evolution and state-of-charge at the single-particle level. High-flux synchrotron radiation and coherent X-rays focusing to micron-scale are essential for isolating diffraction signatures from individual particles embedded within composite electrode films that can exceed 100 µm in thickness and contain tens of thousands of crystallites[25,26].

To isolate and evaluate the limitations intrinsic to electrode architecture, commercially available polycrystalline NMC811 active material was used as received without applying further modifications. Rietveld refinement of NMC811 powder confirms phase purity and low cation disorder (Supplementary Fig. 1). Morphological characterization of NMC811 particles in Supplementary Fig. 2 reveals a hierarchical microstructure which is characteristic of commercial high-Ni layered oxides[27]. The NMC811 powder was cast into thick slurry-processed electrodes containing 90 wt% active material, with an areal loading exceeding 30 mg cm^{-2} and a thickness of ~125 µm, tailored for operando single-particle diffraction measurements as shown in Fig. 1a.

Figure 1b shows the schematic of the experimental setup for the operando single-particle XRD. Coherent X-rays from a synchrotron source were directed through an operando coin cell where the NMC811 thick cathode was being charged to 4.70 V versus Li metal anode at C/10-rate. The coin cell was aligned such that individual Bragg reflections from embedded primary particles within the electrode can be captured on a two-dimensional detector. The detector was shifted to record the (003) Bragg peak of the particles. Figure 1b presents a representative diffraction pattern, in which multiple distinct Bragg reflections are observed along the Debye–Scherrer ring. The magnified region highlights interference fringes surrounding the brightest spot, confirming that the signal originates from a single particle[28].

The electrochemical performance of the cell during the operando X-ray measurements is presented in Fig. 1c. The operando cell delivers a charge capacity approaching 250 mAh g^{-1}, which is close to the theoretical limit of the layered NMC811. The voltage profile without apparent plateau features suggests a solid-solution behaviour, consistent with other reports in the literature[29]. Supplementary Video 1 reveals evolution of the (003) Bragg scattering from NMC811 particles. During early delithiation (up to ~4.25 V), the (003) scattering shifts to lower angles, indicating *c*-axis expansion due to increased electrostatic repulsion between oxygen layers upon Li removal[30]. Above 4.25 V, the Bragg scattering splits and the *c*-lattice collapses, reflecting non-uniform interlayer contraction driven by charge transfer between O 2*p* and partially filled Ni e_g orbitals that reduces oxygen–oxygen repulsion[30].

This asynchronous behaviour is quantitatively revealed in Fig. 1d,e. The *c*-lattice evolution of four representative particles all shows expansion followed by collapse during delithiation but with particle-dependent onset and final *c*-lattice values, indicating distinct states of charge under identical cycling conditions. The onset of scattering broadening (1/Å) likewise varies among particles, reflecting asynchronous development of lattice disorder and microstrain that parallels the *c*-lattice evolution. Together, these results reveal asynchronous delithiation kinetics in slurry-processed thick electrodes under high-voltage cycling—features that are obscured in conventional bulk-averaged XRD measurements.

https://doi.org/10.1038/s41560-026-01981-3

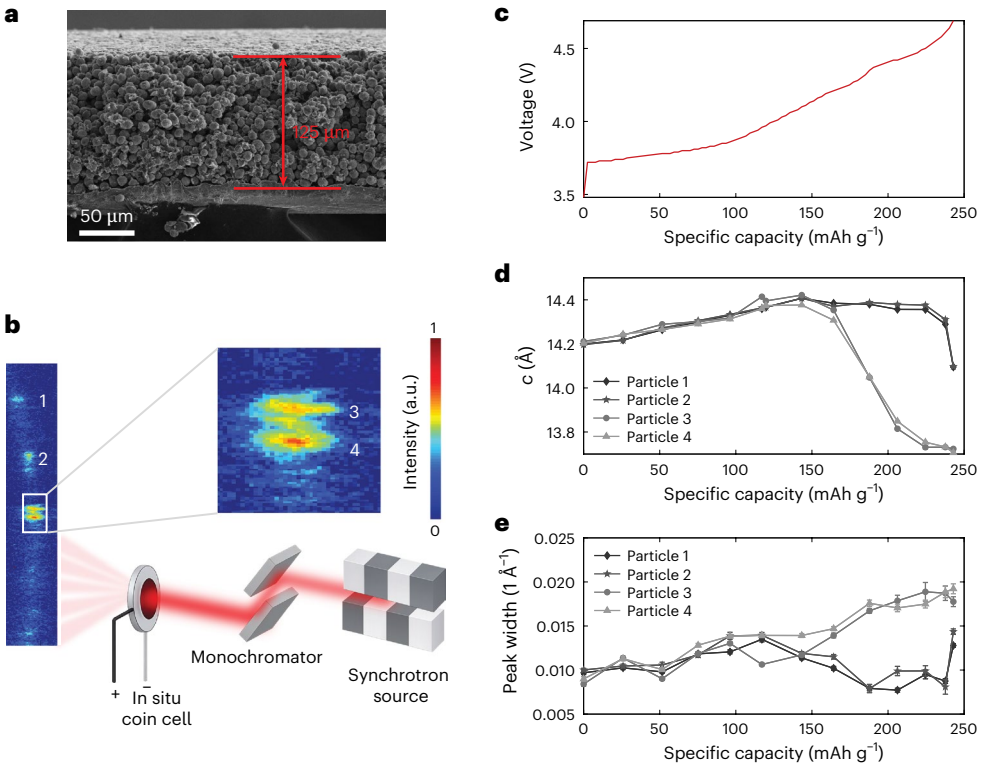

Fig. 1 | Operando single-particle XRD for measuring reaction heterogeneity in thick electrode at high voltage. a, Cross-sectional SEM image of a slurry-processed NMC811 cathode with a total electrode thickness of ~125 µm. **b**, A schematic of the operando single-particle XRD setup using high-flux synchrotron radiation. The colour scale bar represents normalized X-ray intensity scaled by the maximum value in this frame. **c**, Voltage profile for the slurry-processed NMC811 cathode during charging to 4.70 V versus Li metal anode at C/10-rate. The voltage profile shows a charge capacity of ~250 mAh g^{-1}. **d**,**e**, The tracked *c*-lattice parameters obtained from the recorded (003) Bragg peak position (**d**) and (003) Bragg peak widths (**e**) for four representative particles as labelled in **b** reflect asynchronous phase transitions. Data in **d** and **e** are presented as mean values with error bars representing one standard deviation derived from peak fitting for each particle.

To visualize the structural change of the whole ensemble of scattering particles, we angularly averaged all diffraction patterns along the Debye–Scherrer ring and present the resulting intensity profiles under various charging voltages in Fig. 2a. The evolution of the (003) Bragg reflection clearly tracks the expansion and subsequent collapse of the *c*-lattice parameter of NMC811 particles. While all patterns show peak broadening and asymmetry above 4.25 V, the onset of *c*-lattice collapse appears asynchronous across the population of particles. This heterogeneity is reflected by the split and distorted peaks above 4.25 V, which reinforces the earlier single-particle analysis.

Such structural divergence leads to different states of charge or lithium content (that is, x values in $Li_xNi_{0.8}Mn_{0.1}Co_{0.1}O_2$) among particles above 4.25 V, which induces localized overpotentials. This is further supported by Fig. 2b, where increasing the active material ratio from 93 to 97 wt% leads to a clear increase in voltage polarization during charging and discharging. This enhanced polarization indicates aggravated reaction heterogeneity, where spatially uneven state-of-charge distributions emerge as the active material fraction increases. Notably, the 97 wt% electrode shows clear voltage fluctuations near the end of charge, particularly beyond 4.60 V. These irregular features are indicative of asynchronous particle-level reactions, where individual particles or domains reach high states of charge at different times. As a result, the effective utilization of NMC811 decreases with increasing active material ratio, while maintaining the same areal loading of ~30 mg cm^{-2}. Specifically, the reversible capacity drops from 220 mAh g^{-1} at 93 wt% to 200 mAh g^{-1} at 97 wt%, highlighting the limitations of slurry-processed thick electrodes in achieving homogeneous reaction pathways when the active material content exceeds 95 wt%.

Architecture design of dry-processed thick electrode

The observed reaction heterogeneity is not intrinsic to NMC811—being rarely reported in thinner electrodes[29,30] with areal loadings below 3 mAh cm^{-2}—but instead originates from transport limitations in slurry-processed thick electrodes at high voltage. High-voltage charging promotes electrolyte deprotonation, generating acidic byproducts that destabilize the CEI and increase charge-transfer resistance at particle surfaces[17,31]. As the active material content increases, the system becomes increasingly reliant on a well-connected electron percolation network to compensate for these interfacial resistances. Because electron transfer for electrolyte decomposition is facilitated at carbon–electrolyte interfaces, electrode architecture design for high-voltage stability must ensure electronic percolation while minimizing carbon–electrolyte contact area.

Building on these insights, we propose thick electrode architecture design principles to mitigate reaction heterogeneity. These include the use of high-aspect-ratio carbon additives to improve the continuity of the electronic percolation network, minimizing the surface area of conductive carbon to limit direct electron transfer to the electrolyte and engineering interfacial coupling between the insulating binder and conductive carbon. Together, these strategies reinforce conductive network integrity while reducing direct carbon–electrolyte contact area. As shown in Fig. 3a, two structural strategies can be employed to realize effective interfacial coupling: surface coating and fibre-like intertwining. The former refers to the conformal deposition of binder on carbon surfaces; the latter involves fibre-to-fibre entanglement, which requires both the carbon additive and binder to possess fibrous morphology.

The choice of carbon additive is critical for thick electrode design. VGCF exhibits an aspect ratio exceeding 200, with a typical diameter

https://doi.org/10.1038/s41560-026-01981-3

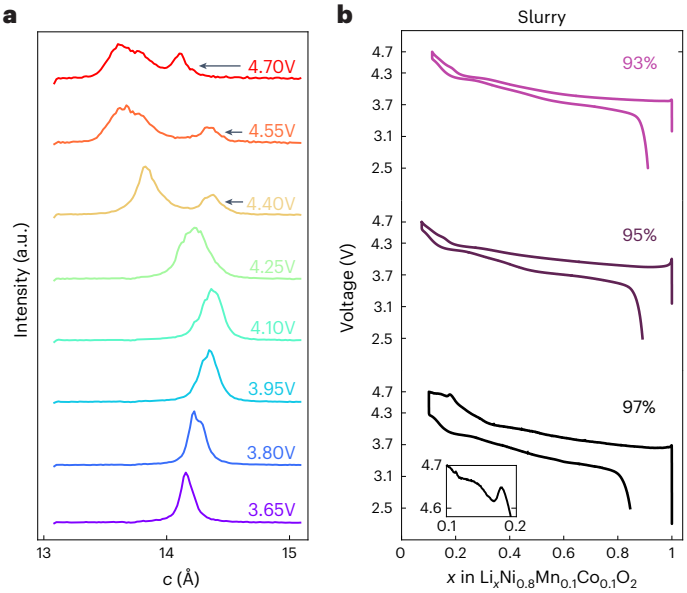

Fig. 2 | Impact of reaction heterogeneity in slurry-processed thick electrode on optimizing active material ratio at high voltage. a, Angularly averaged diffraction patterns along the Debye–Scherrer ring under different charging voltage. The arrows indicate the emergence of a pseudo-peak accompanying the splitting of the (003) Bragg scattering. **b**, Voltage profiles of slurry-processed NMC811 thick electrodes with various active material ratios during charging and discharging between 4.70 and 2.50 V versus Li metal anode at C/10-rate. The inset highlights voltage polarization and fluctuations in the high-voltage region near the end of charge for the slurry-processed thick electrodes with 97 wt% active material.

of ~100 nm and length greater than 20 µm (Supplementary Fig. 3), providing sufficient connectivity for a three-dimensional (3D) percolation network (Supplementary Table 2) while maintaining a low specific surface area (~18.6 $m^2 g^{-1}$), more than ten times lower than that of carbon nanotubes. These properties make VGCF well suited for high-loading cathodes. PTFE is selected as the binder due to its ability to fibrillate under shear during dry processing[32], forming fibre-like structures that entangle with VGCF, reinforce electronic percolation and reduce direct VGCF–electrolyte contact.

Beyond morphological similarity, effective VGCF–PTFE coupling requires chemical interactions. VGCF containing intrinsic surface oxygen functional groups (~1.5 wt% O; Supplementary Table 3) was therefore selected to provide reactive sites. X-ray photoelectron spectroscopy (XPS) reveals a shift in the O 1*s* peak from 533 to 531 eV after dry shear mixing with PTFE (Supplementary Fig. 4), while the C 1*s* peak remains unchanged, indicating a transformation of surface oxygen species rather than charge transfer from the binder. Deconvolution of the O 1*s* spectra (Supplementary Fig. 5) shows that pristine VGCF is dominated by C–O (56.9%) and -OH (43.1%) species with negligible C=O content, whereas after shear mixing the C=O fraction increases to 55.3%, accompanied by decreases in C–O (36.7%) and -OH (8.0%). This chemical evolution is consistent with an enol-to-keto transition of surface -OH groups (Supplementary Fig. 6), facilitated by PTFE and supported by the presence of hydrogen in VGCF (0.2 wt%). Raman spectroscopy (Supplementary Fig. 7) further confirms this transition, with the I_D/I_G ratio increasing from ~0.10 to ~0.20. In addition, the red shift and broadening of the 2D′ overtone (second-order, non-disorder-induced Raman band), together with the suppression and redistribution of O-H stretching modes, are fully consistent with an C–O/-OH to C=O transformation[33]. Together with PTFE fibrillation under shear, this chemical transition promotes interfacial coupling between carbon and binder in dry-processed electrodes.

Dry electrode processing involves three key steps: shear mixing, which establishes the overall electrode architecture; calendering, which compresses the electrode to achieve target density and porosity; and lamination, which bonds the electrode layer to the current collector. Among these steps, shear mixing is the most critical for determining the spatial distribution and interfacial coupling of binder and carbon. Our modelling efforts therefore focus on this step to capture the dynamic evolution of binder–carbon interactions and network connectivity that ultimately dictate charge transport and interfacial stability in the dry electrode.

In this study, we developed a CGMD model focused on the interaction between VGCF and PTFE. VGCF was simplified as linear carbon chains consisting of 30 particles with a radius of 50 nm to capture its high aspect ratio. PTFE was modelled as chains with a length of ~1 µm, each composed of 70 spherical particles representing -[CF_2–CF_2]- segments, consistent with the morphology observed before fibrillation (Supplementary Fig. 3). This modelling employed the classical Lennard–Jones 12–6 potential[34] to describe chemical interactions between PTFE and VGCF particles.

CGMD simulations (Fig. 3b–f) capture PTFE–VGCF interaction evolution under a shear stress of 5 MPa, consistent with experimental dry-processing conditions. Initially (Fig. 3b), PTFE chains are uniformly dispersed in a relaxed configuration, whereas after shear mixing (Fig. 3c) they redistribute and accumulate near VGCF surfaces. This behaviour arises from mass and inertia differences, with lighter PTFE being more readily displaced than the relatively immobile VGCF and is further driven by chemical interactions between the two components. Radial distribution function (RDF) analysis (Fig. 3d) confirms this redistribution, showing increased PTFE probability density near VGCF at $r \approx 60$ nm and a corresponding increase in coordination number after shear mixing. Together, these results demonstrate that shear-induced PTFE redistribution is critical for establishing strong binder–carbon coupling in dry-processed electrodes.

The structural evolution of PTFE during shear mixing was further quantified by the radius of gyration (RoG) distribution (Fig. 3e). Initially, relaxed PTFE chains exhibit a broad RoG peak at ~60 nm, which shifts to ~45 nm after shear mixing, comparable to the VGCF radius (50 nm), indicating PTFE winding around the fibres. This behaviour is supported by morphological evidence (Supplementary Fig. 8), showing PTFE helically wrapped along VGCF surfaces (yellow arrows). In addition, PTFE also forms conformal coating layers on VGCF walls, indicating multiple modes of interfacial coupling in dry-processed electrodes.

During shear mixing, PTFE chains wind around VGCFs via friction and tension, drawing fibres closer and forming a stable conductive network (Fig. 3f). As mixing proceeds, the interfibre distance decreases from ~360 to ~250 nm, reflecting PTFE-mediated connectivity and alignment of VGCFs. To quantify electronic network efficiency, large-area cross-sectional imaging was performed on dry- and slurry-processed thick electrodes (areal loading ~30 mg cm^{-2}) using plasma focused ion beam–scanning electron microscopy (PFIB–SEM), whose high milling rate enables statistically representative sectioning over large areas[17,35]. The resulting PFIB–SEM images were segmented by grayscale contrast into NMC811 active material (red), carbon–binder domain (CBD, dark blue) and pores (light blue), as shown in Fig. 4a,b for dry- and slurry-processed electrodes, respectively.

Conventional analysis often emphasize CBD uniformity across electrode thickness as an indicator of thick-electrode performance. Analysis of segmented PFIB–SEM images (Supplementary Fig. 9) shows comparable CBD uniformity in dry- and slurry-processed thick electrodes, with standard deviations of 1.15% and 1.00%, respectively. However, uniformity alone does not capture conductive network efficiency; instead, CBD connectivity is the primary determinant of effective electronic percolation.

Connectivity maps (Fig. 4c,d), in which each colour represents an isolated CBD subnetwork, reveal sharp differences between the

https://doi.org/10.1038/s41560-026-01981-3

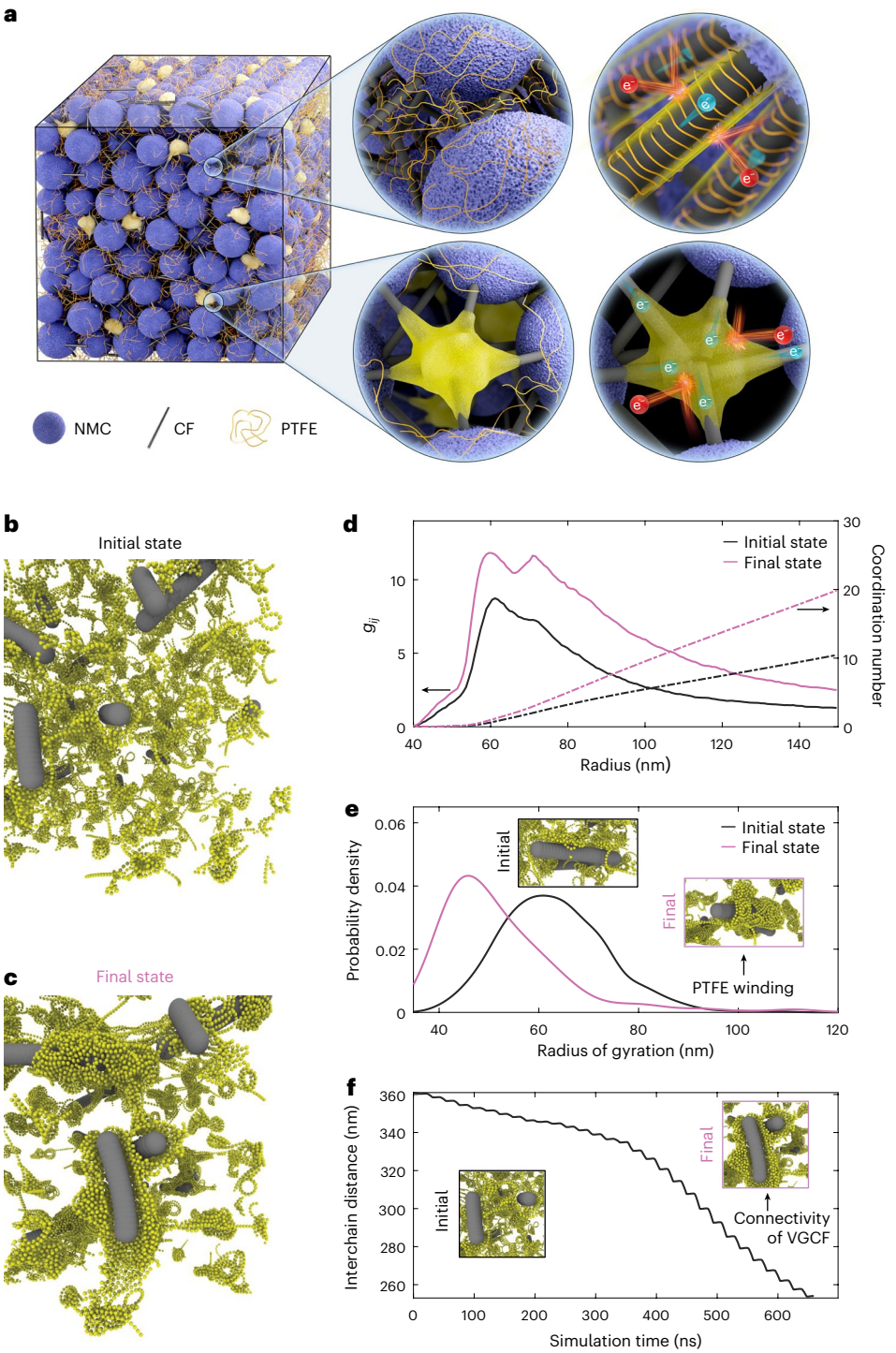

Fig. 3 | Architecture design and modelling verification of dry-processed thick electrode for high-voltage stability. a, A schematic illustration of the composite thick electrode composed of NMC particles, carbon fibres (CF) and PTFE binder. **b**, The initial state of the electrode materials mixture assumed in the modelling. **c**, The final state of the electrode microstructure after performing CGMD simulations. **d**, The calculated RDF distribution between VGCF and PTFE for the initial and final state. g_{ij} is the pair RDF between species VGCF (i) and PTFE (j). **e**, Calculated probability density distribution of RoG for the initial and final state of the PTFE binder. The insets show representative PTFE chain conformations before and after shear mixing, illustrating the transition from a relaxed configuration to a more compact, wrapped state around VGCF. **f**, Calculated evolution of the interchain distance between VGCF pair as a function of the simulation time. The insets display snapshots of VGCF pairs before and after shear mixing, highlighting the progressive reduction in interfibre distance.

two electrodes. In the slurry-processed electrode, the CBD is fragmented, with the largest connected cluster accounting for only 17.1% of total CBD pixels, whereas the dry-processed electrode exhibits a dominant percolating network comprising 61.2%. The 3D PFIB–SEM tomography (Supplementary Fig. 10) over a representative volume (~$100 \times 100 \times 30\ \mu m^3$) confirms this contrast: statistical analysis of labelled subnetworks across slices (Supplementary Fig. 11) shows that the dry-processed electrode not only has a larger dominant CBD fraction on average but also a narrower distribution, indicating more robust and spatially continuous electronic percolation.

https://doi.org/10.1038/s41560-026-01981-3

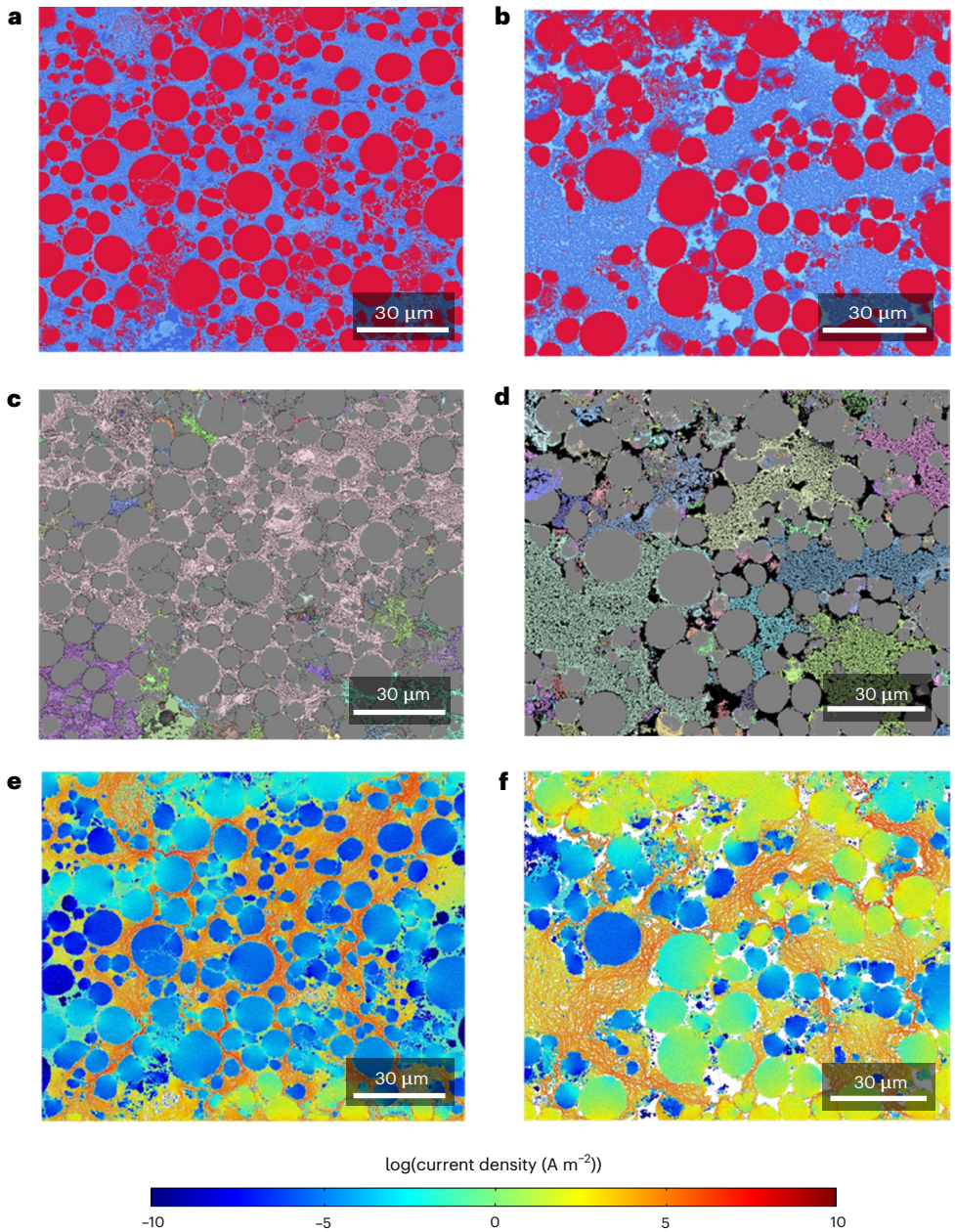

Fig. 4 | Connectivity evaluation of the electronically conductive network for both dry- and slurry-processed thick electrodes with areal loading of ~30 mg cm^{-2}. a,**b**, Segmented PFIB–SEM images of dry- (**a**) and slurry-processed (**b**) electrodes, with the NMC811 in red, the CBD in dark blue and the pores in light blue. **c**,**d**, The connectivity maps of the CBD network, and the different colours represent different aggregates of CBD, for the dry- (**c**) and slurry-processed (**d**) electrodes. **e**,**f**, Distribution of the simulated current density in the NMC811 active material and CBD with a current equivalent to C/3-rate flowing from top to bottom for the dry- (**e**) and slurry-processed (**f**) electrodes.

To quantify the impact of CBD connectivity, current flow equivalent to C/3 was simulated across the electrode thickness (Fig. 4e,f). In the slurry-processed electrode, a larger fraction of current passes through NMC811 particles, yielding an average particle current density of 1.0×10^{-2} A m^{-2}, compared with 4.6×10^{-5} A m^{-2} for the dry-processed electrode. Because NMC811 has electronic conductivity approximately five orders of magnitude lower than the CBD, this parasitic current flow leads to increased ohmic losses. These results demonstrate that the superior CBD connectivity in dry-processed thick electrodes promotes electronic transport through the most conductive phase, enabling more homogeneous utilization of NMC811 under high-voltage operation. Beyond electronic transport, Li^+ transport through the electrolyte has also been identified as a kinetic limitation in thick electrodes[36,37]. To quantitatively assess its contribution, we then evaluated the ionic transport parameters of both slurry- and dry-processed electrodes. Both electrodes exhibit comparable pore distribution uniformity: standard deviation 0.89% for slurry and 1.2% for dry (Supplementary Fig. 12), which indicates no porosity-induced penalty. However, the dry-processed electrode shows reduced tortuosity (2.49 versus 2.87), corresponding to an ~13% decrease and an ~33% increase in effective Li^+ diffusivity relative to the slurry-processed electrode (Supplementary Fig. 13). This reduced tortuosity contributes to improved ionic transport, complementing the enhanced electronic percolation in dry-processed thick electrodes.

Dry-processed thick electrode for high-voltage stability

In the dry-processed electrode, PTFE binder winds around and coats VGCF fibres through shear-driven chemical interactions, simultaneously

https://doi.org/10.1038/s41560-026-01981-3

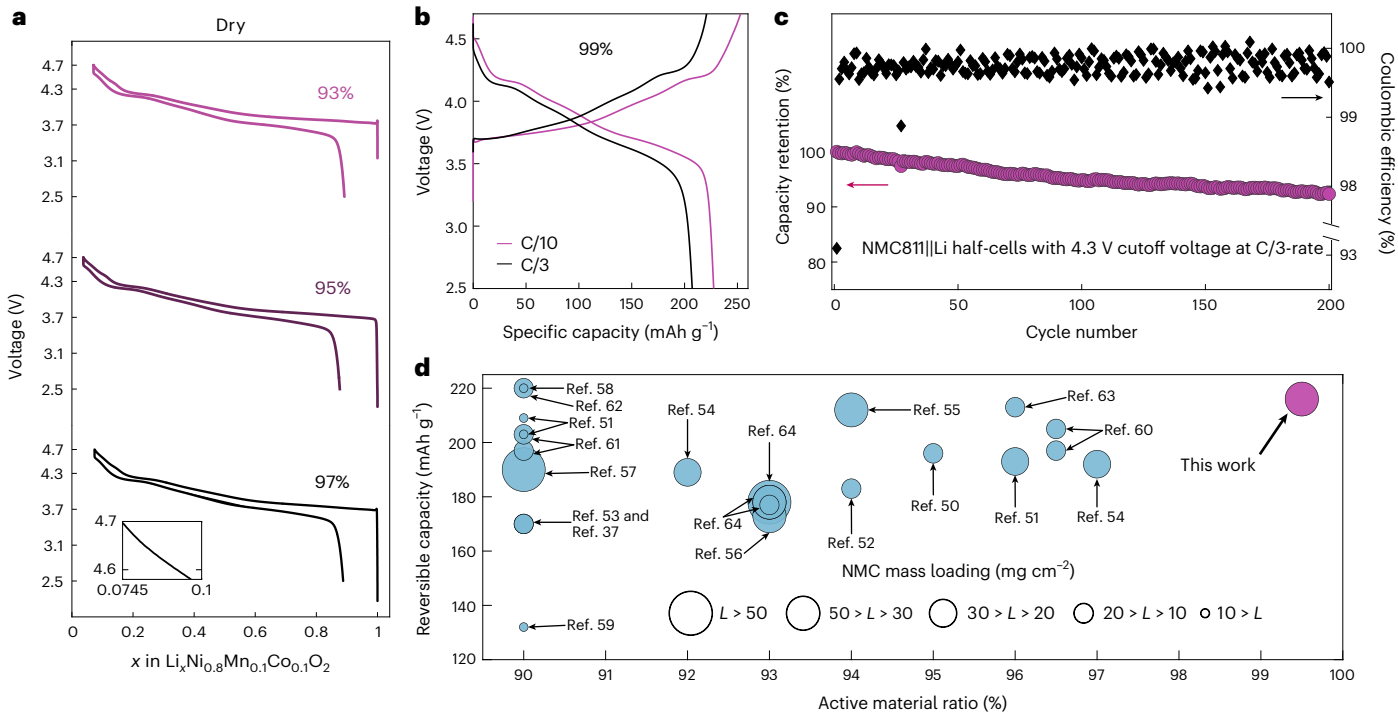

Fig. 5 | Electrochemical performances of dry-processed thick electrode demonstrating high-voltage stability and maximized active material content. a, Voltage profiles of dry-processed NMC811 thick electrodes (areal loading of ~30 mg cm^{-2}) with various active material ratios during charging and discharging between 4.70 and 2.50 V versus Li metal anode at C/10-rate. The inset highlights a smooth voltage profile in the high-voltage region near the end of charge for the dry-processed thick electrodes with 97 wt% active material. **b**, Voltage profiles of dry-processed NMC811 thick electrodes with 99 wt% active material during C/10- and C/3-rate cycling versus Li metal anode. **c**, Cycling performances of NMC811 dry-processed thick electrodes with 99 wt% active material at C/3-rate versus Li metal anode. The pink arrow points to the *y* axis showing the capacity retention and the black arrow points to the *y* axis showing the Coulombic efficiency. **d**, Literature results summary of electrochemical performance for high-Ni NMC layered cathodes with varying active material contents[37,50–64] (see Supplementary Table 5 for all performances and cell parameters). *L* stands for mass loading.

enhancing electronic connectivity and forming a barrier that suppresses direct carbon–electrolyte contact, thereby mitigating electrolyte decomposition at high voltages. This binder–carbon coupling is absent in slurry-processed electrodes. Linear sweep voltammetry (LSV) confirms that, despite using the same VGCF additive, slurry-processed composites exhibit an earlier onset of parasitic reactions and higher currents than dry-processed counterparts (Supplementary Fig. 14).

Consequently, increasing the active material content from 93 wt% to 97 wt% in the dry-processed electrode (Fig. 5a), while maintaining a high areal loading of ~30 mg cm^{-2} and a cutoff voltage of 4.70 V, does not introduce additional overpotential during the initial cycle at C/10-rate, and the reversible capacity remains stable at ~220 mAh g^{-1}. Unlike slurry-processed thick electrodes, which show voltage fluctuations above 4.60 V due to asynchronous particle-level reactions, dry-processed electrodes display smooth voltage profiles across all active material ratios, indicating homogeneous delithiation. This advantage extends to ultrahigh loadings, with areal capacities approaching 9 mAh cm^{-2} (areal loading ~45 mg cm^{-2}) exhibiting voltage profiles nearly identical to those at lower loadings (Supplementary Fig. 15).

Operando single-particle XRD was performed on dry-processed thick electrodes during charging to 4.70 V (Supplementary Fig. 16). Individual NMC811 particles show continuous angular shifts of the (003) Bragg scatterings throughout charging (Supplementary Video 2), indicating synchronous lattice evolution across the ensemble. Unlike slurry-processed electrodes, no peak splitting or pronounced broadening is observed above 4.25 V (Supplementary Fig. 17), implying minimized state-of-charge heterogeneity and suppressed local overpotentials. Electrochemical impedance spectroscopy (EIS) further shows consistently lower resistance for dry-processed electrodes cycled to 4.70 V (Supplementary Fig. 18 and Supplementary Table 4). These results confirm that reaction heterogeneity in slurry-processed thick electrodes originates from electrode architecture rather than intrinsic NMC811 properties. By mitigating Li concentration gradients within particles and across the electrode, the dry-processed electrode achieves a Li^+ diffusivity of 6.9×10^{-12} cm^2 s^{-1}, more than four times higher than that of the slurry-processed electrode.

Building on these results, the active material content was further increased to 99 wt% in dry-processed electrodes while maintaining an areal loading of ~30 mg cm^{-2}. The resulting free-standing films (~25 cm^2) exhibit excellent flexibility and structural integrity, remaining crack-free upon bending (Supplementary Fig. 19), which is essential for roll-to-roll manufacturing[38]. Mechanical testing (Supplementary Fig. 20) further confirms despite increasing the active material fraction from 93 wt% to 99 wt%, the tensile strength remains comparable to thick electrodes using substantially higher binder contents[39].

Electrochemically, the 99 wt% dry-processed electrode delivers exceptional performance (Fig. 5b). At C/10, the first charge capacity reaches 253 mAh g^{-1} (93% of the theoretical capacity of NMC811), with a discharge capacity exceeding 225 mAh g^{-1} and an initial Coulombic efficiency (CE) of 89%. At C/3, a high specific capacity of ~210 mAh g^{-1} is retained. Rate capability tests (Supplementary Fig. 21) show negligible voltage polarization up to 6.0 mA cm^{-2} for both charge and discharge, with polarization at higher rates primarily attributed to limitations of the Li metal anode paired with the high-loading cathode (~30 mg cm^{-2}) in carbonate electrolytes[40,41]. Importantly, increasing the active material content from 93 wt% to 99 wt% does not reduce the NMC–CBD contact fraction (Supplementary Fig. 22), confirming preserved percolation integrity.

https://doi.org/10.1038/s41560-026-01981-3

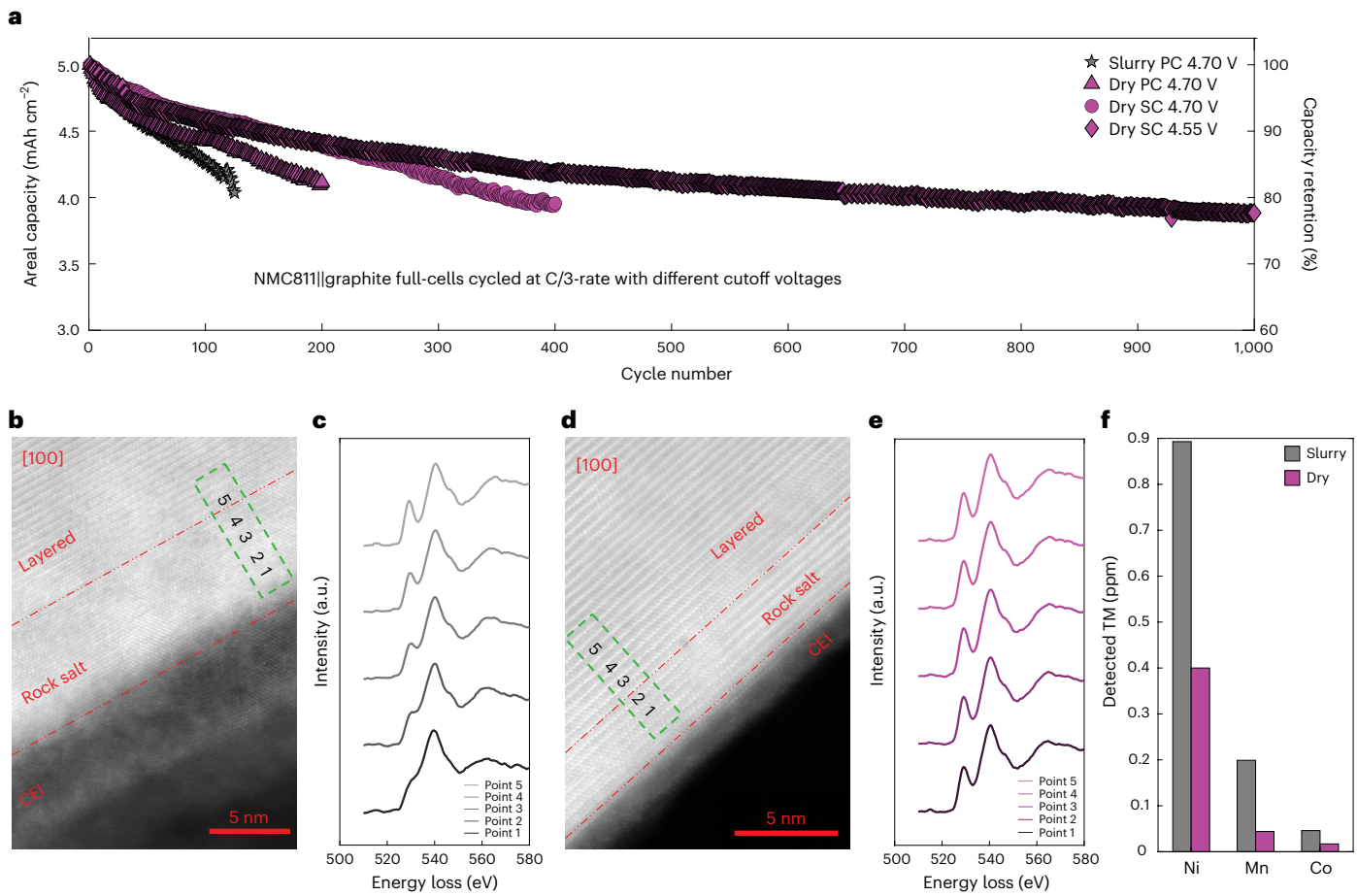

Fig. 6 | Comparison of electrochemical performance and post-mortem analysis of thick electrode applied in NMC811||graphite full cells highlighting the high-voltage stability of dry-processed electrodes. a, Cycling performance of full cells using 95 wt% NMC811 cathodes (areal loading of ~5 mAh cm^{-2}) at C/3-rate. Both *y* axes correspond to the same electrochemical data for all cases. The left *y* axis reports the absolute areal capacity to show the magnitude of capacity decay, whereas the right *y* axis presents the corresponding capacity retention, normalized to the initial areal capacity for convenience of comparison. Note that the SC 4.55 V case was evaluated using pouch-type full cells, whereas the remaining three cases were tested using coin-type full cells. PC, polycrystalline; SC, single crystal. **b**, Aberration-corrected STEM-HAADF image of NMC811 particles in the slurry-processed electrode after 100 cycles. **c**, Spatially resolved O K-edge EELS spectra from surface to bulk of NMC811 particles in the slurry-processed electrode after 100 cycles. **d**, Aberration-corrected STEM-HAADF image of NMC811 particles in the dry-processed electrode after 100 cycles. **e**, Spatially resolved O K-edge EELS spectra from surface to bulk of NMC811 particles in the dry-processed electrode after 100 cycles. The points 1–5 in **c** and **e** correspond directly to the labelled numbers within dashed green boxes in **b** and **d**, respectively. **f**, ICP-MS analysis of graphite anodes paired with thick NMC811 cathodes after 100 cycles. TM, transition metal.

Cycling stability was evaluated in Li-metal half-cells using a liquefied gas electrolyte and a reduced cutoff voltage of 4.30 V to mitigate Li–electrolyte incompatibility[42]. As shown in Fig. 5c, the 99 wt% electrode retains 92% of its initial capacity over 200 cycles with an average CE exceeding 99.7%. Pushing the design further, electrodes with 99.5 wt% active material (Supplementary Fig. 23) maintain a high discharge capacity of 216 mAh g^{-1} and outperform reported benchmarks (Supplementary Table 5). The bubble chart in Fig. 5d highlights the unique combination achieved here—ultrahigh active material content (~99.5 wt%), high mass loading (~30 mg cm^{-2}) and high reversible capacity—surpassing most literature reports clustered at 90–94 wt% with lower loadings.

High-voltage full-cell performance was then assessed using graphite anodes. Under a cutoff voltage of 4.70 V at C/3, slurry-processed NMC811||graphite cells show rapid degradation, with areal capacity retention dropping to 85% after 100 cycles and 80% after 125 cycles (Fig. 6a). By contrast, dry-processed full cells retain 89% of their initial areal capacity (~5 mAh cm^{-2}) after 100 cycles and 82% after 200 cycles, with a higher average CE of 99.89% compared with 99.74% for slurry-processed cells (Supplementary Fig. 24). Even under harsh conditions—cycling at 50 °C with a 4.70 V cutoff—the dry-processed NMC811 retains 72% of its areal capacity after 100 cycles (Supplementary Fig. 25), highlighting its advantage under simultaneous high-temperature and high-voltage stress.

To elucidate high-voltage degradation mechanisms, aberration-corrected scanning transmission electron microscopy in high-angle annular dark field mode (STEM-HAADF) was performed on NMC811 particles collected from thick electrodes after 100 cycles. The slurry-processed electrode exhibits a non-uniform CEI exceeding 5 nm, with porous regions and discontinuities indicative of electrolyte-driven interfacial corrosion (Fig. 6b). By contrast, the dry-processed electrode maintains a compact, uniform CEI with an average thickness of ~2 nm (Fig. 6d), consistent with more effective interfacial passivation.

Electron energy loss spectroscopy (EELS) line scans were acquired from surface to bulk of the particles to probe the local electronic structure evolution. The spatially resolved O K-edge spectra reveal pronounced suppression of the oxygen pre-edge feature (~532 eV) near the surface of slurry-processed particles, disappearing entirely within the rock-salt region (Fig. 6c), indicating oxygen loss and transition-metal dissolution associated with layered-to-rock-salt transformation[43]. By comparison, the dry-processed electrode retains the oxygen pre-edge feature across the surface-to-bulk region (Fig. 6e), confirming better preservation of the layered structure after cycling.

This improved structural stability arises from the dry-electrode architecture, which facilitates electronic connectivity while limiting direct carbon–electrolyte contact, thereby suppressing high-voltage parasitic reactions and electrolyte decomposition. Reduced formation of acidic species such as HF mitigates CEI corrosion, oxygen loss and transition-metal dissolution[44]. Inductively coupled plasma mass spectrometry (ICP-MS) of cycled graphite anodes (Fig. 6f) confirms substantially higher transition-metal deposition—primarily Ni—in cells with slurry-processed cathodes, implying severe cathode–anode crosstalk that accelerates lithium inventory loss[3].

To further extend high-voltage stability, single-crystal NMC811 (Supplementary Fig. 26) was employed to reduce surface area and mitigate grain-boundary cracking. The dry-processed electrode using single crystal demonstrates improved cycling stability at a 4.70 V cutoff, retaining nearly 80% of its initial areal capacity after 400 cycles with an average CE of 99.91% (Fig. 6a), highlighting the compatibility of the dry-processing strategy with single-crystal morphologies.

The trade-off between energy density and cycling stability was further evaluated by varying the voltage cutoff (Supplementary Fig. 27). Increasing the cutoff from 4.20 to 4.70 V raises the material-level discharge energy density from 701 to 868 Wh kg^{-1}, corresponding to a 23.8% gain (Supplementary Table 6), while a 4.60 V cutoff already delivers a 21.8% increase. Guided by this analysis, we evaluated a dry-processed NMC811||graphite full pouch cell with a 4.55 V cutoff. As shown in Fig. 6a, this cell achieves excellent cycling stability, retaining 78% of its initial areal capacity after 1,000 cycles at a C/3-rate, with an average CE of 99.92%.

Post-mortem scanning electron microscopy (SEM) analysis of graphite anodes (Supplementary Fig. 28) shows intact particles after long-term cycling, with no fracture or exfoliation and only edge smoothing due to surface solid electrolyte interphase accumulation. Finally, benchmarking against prior reports (Supplementary Fig. 29) demonstrates that, unlike most high-mass-loading electrodes (≥25 mg cm^{-2}) that fade within 200–400 cycles, the dry-processed NMC811||graphite pouch cell sustains stable operation well beyond 1,000 cycles.

Conclusion

In this work, we report a design principle for maximizing active material content in thick electrodes operating under high voltage. High-aspect-ratio VGCF form an interconnected electronic network that efficiently links active material particles, whereas fibrillated PTFE binder coats and stabilizes these carbon fibres, maintaining pathway integrity and reducing direct carbon–electrolyte contact to suppress parasitic reactions. Central to this design is the interfacial coupling between PTFE and VGCF, enabled by an enol-to-keto transition during dry processing. This chemical transformation, facilitated by shear stress, lays the molecular foundation for a robust architecture under high-voltage operation. As a proof of concept, the dry-processed NMC811 cathode with ~30 mg cm^{-2} loading and 99 wt% active material enables stable operation up to 4.70 V. Full cells with a 4.55 V cutoff and 5 mAh cm^{-2} areal capacity sustain 1,000 cycles with an average CE above 99.9%. This work also indicates efficient electronic transport depends on network connectivity rather than uniformity alone, and the conventional view that conductive carbon and binder serve isolated roles must be re-evaluated. Their synergistic interaction is essential for achieving both structural integrity and electrochemical stability.

Methods

Thick electrode fabrication

Dry-processed electrodes were prepared by mixing commercial NMC811 powder (polycrystalline from Targray or single crystal from MSE Supplies), PTFE binder (Chemours) and VGCF (Sigma-Aldrich) at a specified mass ratio. A conductive carbon-to-binder mass ratio of 5:2 was consistently adopted for all slurry-processed and dry-processed electrodes, except in the ultrahigh active material case (99.5 wt%), where the formulation was adjusted to 0.4 wt% VGCF and 0.1 wt% PTFE. The dry mixture was shear mixed at 100 °C for 10 min under an applied shear stress in the range of 1–5 MPa to form a cohesive free-standing film. To achieve target thickness and porosity of ~30%, the film was rolled on a 100 °C hot plate and subsequently hot-calendered at 100 °C onto 20-µm etched aluminium foil (Tob New Energy). The final NMC811 mass loading was ~30 mg cm^{-2} for half-cell testing and ~25 mg cm^{-2} for full-cell testing, corresponding to ~6 and ~5 mAh cm^{-2}, respectively. For comparison, the slurry-processed thick NMC811 electrodes were fabricated by doctor blade method[45]. Polyvinylidene fluoride (PVDF, Arkema) was first dissolved in *N*-methyl-2-pyrrolidone (Sigma-Aldrich) using a planetary mixer (ARE-310, Thinky) for 10 min. NMC811 powder and conductive agent were then added at the desired mass ratios and mixed for an additional 1 h to form a homogeneous slurry. The slurry was cast onto aluminium foil using a doctor blade with a defined gap thickness and dried under vacuum at 60 °C overnight to remove *N*-methyl-2-pyrrolidone, followed by further drying at 120 °C for 1 h.

Half-cell testing

Electrodes with a 0.5-inch diameter were punched and dried in a vacuum oven at 100 °C for 24 h. In half-cell configurations, lithium metal (Tob New Energy) was used as the counter electrode, with Celgard 2325 as the separator for electrodes with ~6–9 mAh cm^{-2} areal capacity. The areal capacity is defined by the discharge specific capacity at the formation cycle times the active material areal loading in each case. CR2032 coin cells were assembled using 0.5-mm-thick spacer and one spring at the anode side. A Gen2 electrolyte (1 M $LiPF_6$ in EC:EMC of 3:7 by weight, Gotion) was used for reversible capacity measurements and C-rate performance testing. Galvanostatic cycling was performed at various C-rates with 1C defined as 180 mA g^{-1} and a voltage window of 2.50–4.70 V. For extended cycling stability studies, a liquefied gas electrolyte composed of 1.2 M LiTFSI and 1 M acetonitrile in fluoromethane:CO_2 (19:1 by weight) was used, with an additional 5 wt% CO_2 to enhance Li-metal stability[42]. For each testing condition, three half cells were evaluated to make sure reported results are representative.

Full-cell testing

Both CR2032 coin cells and pouch cells were assembled for full-cell testing. All full-cell measurements with a 4.70 V cutoff were carried out in CR2032 coin-cell format, whereas the cycling tests at a 4.55 V cutoff were performed using a pouch-cell configuration. Graphite electrodes (94 wt% active material) provided by the Ningbo Institute of Materials Technology and Engineering were used as the anode using the same industrial-scale coating and calendaring equipment employed for commercial electric vehicle-grade lithium-ion battery production. The single-side areal capacity is 6.0 ± 0.2 mAh cm^{-2} for an N/P ratio of 1.1–1.15. For single-layer pouch cells, cathodes measured 44 mm × 30 mm and anodes 45 mm × 32 mm. Initial assembly was conducted without electrolyte in ambient atmosphere. The sealed pouches were transferred to a heating tray in the glovebox antechamber and vacuum-dried at 80 °C overnight. After drying, the cells were moved into an Ar-filled glovebox for electrolyte injection, avoiding air exposure. Electrolyte filling was controlled at a ratio of 3 g Ah^{-1}, using an all-fluorinated electrolyte (1 M $LiPF_6$ in FEC:FEMC of 3:7 by weight). Celgard 2325 served as the separator. The pouch-type full-cell cycling in this study was conducted under a constant stack pressure of 350 kPa, calculated based on the projected area of the graphite electrode. A thin load cell positioned directly above the pouch cell continuously monitored the applied pressure throughout long-term cycling. Cells were cycled at C/10-rate for the first two cycles, followed by extended cycling at C/3-rate in the voltage range of 2.50–4.70 V or 2.50–4.55 V. The reversible capacity for the 4.55 V NMC811||graphite pouch cell was 66 mAh at C/10-rate. The electrochemical tests were performed at either 25 °C or 50 °C using a Neware Battery Test System (Neware). For

each testing condition, three coin-type full cells or two pouch-type full cells were evaluated to make sure reported results are representative.

LSV measurements

LSV was performed using a BioLogic VSP-300 at a scan rate of 1 mV s^{-1}, sweeping from open-circuit voltage to 4.80 V in a half-cell configuration. The working electrode consisted solely of VGCF and binder:polyvinylidene fluoride was used for the slurry-processed electrode, whereas PTFE was employed for the dry-processed electrode. For fair comparison, the reported parasitic currents were normalized by the electrode mass.

EIS measurements

EIS measurements were performed using a BioLogic VSP-300 on half-cells with NMC811 thick electrodes prepared via either dry or slurry processing with 95 wt% active material. An applied AC potential of 10 mV over a frequency range from 1 MHz to 1 mHz was used. Impedance analysis was performed after cycling with a charging cutoff voltage of 4.70 V using a classical equivalent circuit model[46] (Supplementary Fig. 18), where R_s (R1), R_{sei} (R2) and R_{ct} (R3) represent the electrolyte, interphase and charge-transfer resistances, respectively. We extracted the low-frequency Warburg coefficient and calculated the solid-state lithium diffusivity using the following equation:

$$D_{EIS} = \frac{1}{2}\left(\frac{RT}{z^2F^2CAR_w}\right)^2,$$

where R is the ideal gas constant, T is the absolute temperature, z is the number of electrons transferred in the redox reaction, F is the Faraday's constant, C is the lithium concentration, A is the electrode surface area and R_w is the Warburg coefficient.

Powder XRD

NMC811 powders (either polycrystalline from Targray or single-crystal from MSE Supplies) were sealed in boron-rich glass capillary tubes (0.7 mm diameter, Charles Supper Company) within an Ar-filled glovebox maintained at <0.1 ppm H_2O. XRD measurements were conducted using a Bruker APEX II Ultra diffractometer operated at 50 kV and 50 mA. Rietveld refinement was applied to the collected XRD data to determine the lattice parameters and site occupancies of the pristine samples.

Operando single-particle XRD

Operando single-particle XRD measurements were performed using 9.0 keV photons on a half-cell setup, with diffraction patterns collected by a charge-coupled device positioned 0.5 m downstream from the sample. The coin cell casing was modified with a 5 mm opening sealed by Kapton film on both sides, allowing X-ray transmission without compromising electrochemical performance. NMC811 cathodes, prepared via either dry or slurry processing with 90 wt% active material, were used. The detector was positioned at a fixed 2θ angle to monitor the (003) Bragg reflection from randomly oriented nanoparticles. The incident beam was defined to 20 μm × 20 μm by slits. Since the overall crystallographic symmetry remains unchanged during cycling, tracking the (003) peak position provides sufficient insight into structural evolution.

Surface characteristics analysis

XPS was conducted on VGCF samples before and after dry mixing with PTFE under shear stress using a Kratos AXIS Supra system. Measurements were performed with a monochromatic Al Kα source (15 kV) under a vacuum of ~10^{-8} Torr. An automatic charge neutralizer was used during data acquisition. Survey spectra were collected with a 1.0 eV step size, followed by high-resolution scans at 0.1 eV intervals. All spectra were calibrated to the C 1*s* peak at 284.6 eV. Peak fitting using CasaXPS software was performed after Shirley background subtraction. Mixed Gaussian–Lorentzian line shapes were used for the peak fitting with full width at half maximum and peak positions constrained consistently across samples to enable quantitative comparison of surface chemical states.

Raman spectroscopy analysis

Raman spectroscopy was performed on VGCF samples before and after dry mixing with PTFE under shear stress using LabRAM HR Evol Raman Microscope. The samples were sealed between two very thin transparent glass slides. The measurements were run using a 532-nm laser source, 600 gr/mm grating from a wavenumber range between 50 and 3,500 cm^{-1}.

Chemical composition analysis

Elemental analysis of VGCF was performed by Midwest Microlab. Carbon, hydrogen and nitrogen contents were measured using Dumas combustion, in which the sample was fully oxidized in O_2 at ~950–1,050 °C and the resulting CO_2 and H_2O were quantified by thermal conductivity or infrared detection against certified standards (for example, acetanilide). Oxygen content was analysed using a dedicated LECO-type oxygen module via inert pyrolysis at ~1,060 °C under He flow, converting oxygen to CO for subsequent catalytic conversion and quantification. The transition-metal contents on cycled graphite electrodes were quantified using ICP-MS (iCAP RQ, Thermo Fisher Scientific). Graphite electrodes collected from coin cells after 100 cycles were punched into 1/8-inch discs and soaked overnight in 3 mol l^{-1} H_2SO_4 for transition-metal extraction. The resulting supernatant was collected and appropriately diluted for ICP-MS analysis.

Mechanical properties measurements

Dry electrodes were fabricated into rectangular strips and subsequently cut into dogbone specimens using a 3D-printed stencil (gauge section 0.6 cm × 1.2 cm). The thickness of each specimen was measured with a micrometre before testing. To localize fracture within the gauge region, the two gripping ends were reinforced with electrical tape. Tensile measurements were conducted on a linear actuator (ESM303, Mark-10) equipped with a 10 N force gauge, using 3D-printed grips, at an elongation rate of 1 mm min^{-1} until mechanical failure.

Modelling for shear mixing process

To investigate the mesoscale interactions between PTFE binder and VGCF, we performed CGMD simulations. Particle size and mass were calibrated based on material density to ensure a physically realistic environment. Each PTFE chain was modelled as a 1,035 nm polymer comprising 70 coarse-grained beads, with each bead representing several $-[CF_2-CF_2]-$ units and a radius of 14 nm. VGCF was simplified as a linear chain of 30 carbon beads with 50 nm radius each, representing the overall carbon structure and surface. The simulation system included 10 VGCF chains and 500 PTFE chains to capture their interfacial behavior.

Interactions were assumed to be governed by the classical 12–6 Lennard–Jones (LJ) potential, with parameters adapted from the Martini 3 force field[34]

$$V_{LJ}(r) = 4\varepsilon\left[\left(\frac{\sigma}{r}\right)^{12} - \left(\frac{\sigma}{r}\right)^{6}\right].$$

Here, ε represents the potential well depth and σ the distance at which potential energy is zero. Notably, the interaction strength (ε) between VGCF and PTFE was set higher than that between PTFE chains, reflecting stronger binding—consistent with enol-to-keto transformations observed experimentally. A harmonic potential was also applied to model bond length and angle variations within the PTFE chain.

Simulations were conducted in a 1.5 × 1.5 × 1.5 μm^3 periodic box using the LAMMPS package[47]. The system underwent a 50 ns pre-equilibration

at 300 K (NVT ensemble), followed by heating to 373.15 K for 10 ns. Shear mixing was simulated using periodic directional forces (~5 MPa, aligned with experimental shear stress) alternating along $\pm x$, $\pm y$ and $\pm z$ directions for 12 ns per cycle, repeated over 30 cycles. Postshearing relaxation was performed at 373.15 K for 25 ns. To evaluate structural evolution, data were averaged from the initial and final 50 frames of the shear mixing process. Visualization was carried out using OVITO[48].

PFIB–SEM

A Thermo Scientific Helios 5 Laser-PFIB microscope was used for large-area cross-section preparation on NMC811 cathode and followed by Thermo Scientific Apreo 2S scanning electron microscope for imaging. The dry- or slurry-processed cathode with 93 wt% active material was first cut via razor blade before mounting on a 54° pretilted holder for laser and focused ion beam milling. First, the sample was tilted at −6° with its surface at an angle of −60° normal to the incident laser beam. Initial rough laser ablation operations were conducted by utilizing a laser with a power of 1.5 W for two passes of a box pattern, completed within a time frame of 15 s. Then a gentle polishing with laser at a lower power (0.375 W) was conducted via four passes of a box pattern for 40 s. To further improve the polishing quality and remove the laser-induced periodic surface structures, a 5 min automatic rocking mill technology was executed via PFIB at a focused ion beam acceleration voltage of 30 kV and beam current 200 nA. Thermo Scientific Maps software automates the acquisition of a series of tiled images with Apreo 2S SEM to create an overview of the cross-section of samples with in-lens T1 detector under 2 kV accelerating voltage and 25 pA beam current.

To enable image binder within the bulk of the cathode sample without cross-polishing, the sample was broken off in a cryogenic environment via liquid nitrogen (−196 °C), to result in fractured surface. The fractured surface morphology and characteristics were analysed via Thermo Scientific Apreo 2S scanning electron microscope. A low accelerating voltage of 2 kV and 25 pA beam current were set in Optiplan mode with the in-lens detectors (T2 and T3) to image the VGCF and PTFE binder. To further enhance topographical signal, a much lower accelerating voltage of 500 eV and 6.3 pA beam current was set in Immersion mode with beam deceleration to image the VGCF and PTFE binder.

A 3D PFIB–SEM tomography for the dry- and slurry-processed cathode with 93 wt% active material was performed using a Thermo Scientific Helios Hydra PFIB–SEM equipped with the Auto Slice & View 5 (AS&V 5) software. Each 3D volume covered approximately 100 µm × 100 µm × ~30 µm. Before serial sectioning, sample preparation followed the standard AS&V 5 workflow, including the creation of fiducial markers (milling current: 60 nA), milling of front and side trenches (2.5 µA) and final cross-section cleaning (60 nA). The automated slice-and-view acquisition was then conducted at an ion beam accelerating voltage of 30 kV, a milling current of 60 nA and a slicing interval of 250 nm.

Image reconstruction, processing, segmentation and visualization were carried out using Avizo software. The PFIB–SEM slice stack was imported into Avizo and reconstructed with the DualBeam 3D Wizard module. Initial manual segmentation was performed on five representative slices to generate a training set for three-component segmentation (including cathode active material, CBD and pores), followed by deep-learning-based segmentation applied to the entire dataset. To eliminate small isolated artefacts and noise, the opening module was applied to each slice of the segmented CBD. Finally, each subvolume corresponding to the CBD cluster was individually labelled and visualized in distinct colours on each slice. The area fraction of each CBD cluster was analysed for each 3D PFIB–SEM slice to obtain the distribution and fraction of the largest CBD network on each slice.

CBD network quantification

Based on the PFIB–SEM images, the Weka Trainable tool within Fiji was used to segment the image into three phases—the active material, the CBD and the pores. Based on those segmented images, the CBD aggregates were formed if all the CBD pixels within the aggregate were in contact with at least one other CBD pixel part of the aggregate. The contact was investigated with the eight neighbours method within MATLAB. The extent of contact between CBD and NMC active material was quantified by computing the fraction of NMC pixels directly interfacing with CBD pixels via a standard four-neighbour connectivity algorithm.

Electronic current simulation

The segmented PFIB–SEM images were then meshed using the open-access Iso2Mesh toolbox within MATLAB into a 3D mesh of ~5 million of tetrahedra (by stacking two identical images together) and imported into COMSOL Multiphysics 5.6, where the applied parameters are listed in Supplementary Table 7. The equations are listed below:

$$J = \sigma E + \frac{\partial D}{\partial t} + J_{\text{app}},$$

$$E = -\nabla V,$$

$$\text{At the top surface} : J = J_{\text{app}},$$

$$\text{At the bottom surface (current collector)} : J = -J_{\text{app}} \times \frac{\text{Surface}_{\text{top}}}{\text{Surface}_{\text{CC}}}, V = 0.$$

where J is the current density, J_{app} is the current density applied and D is the dielectric displacement.

Tortuosity evaluation

The tortuosity values for each case were computed thanks to the MATLAB add-on 'TauFactor'[49]. The segmented PFIB–SEM images were fed to this add-on, which computed the tortuosity values through a diffusion-based algorithm. Supplementary Fig. 13 illustrates the impact of the difference observed in tortuosity values between the dry- and slurry-processed electrode might have on the Li^+ transport through the electrolyte. The blue curve represents the Bruggeman relation with the phase proportion, which is the electrolyte amount, neglected since they are similar between the dry and slurry cases.

Scanning transmission electron microscopy–EELS

To prepare TEM samples, cycled electrode materials were dispersed onto lacey carbon grids within an Ar-filled glovebox. All loading and transfer procedures were carefully conducted to avoid air exposure. STEM and EELS were performed on primary particles in ADF mode using a JEOL JEM-ARM300CF microscope operated at 300 kV and equipped with dual aberration correctors. To minimize beam-induced damage, EELS spectra were acquired exclusively from regions free of prior electron irradiation.

Reporting summary

Further information on research design is available in the Nature Portfolio Reporting Summary linked to this article.

Data availability

All data generated or analysed during this study are included in the article and its Supplementary Information. Source data are provided with this paper.

References

1. Liu, J. et al. Pathways for practical high-energy long-cycling lithium metal batteries. *Nat. Energy* **4**, 180–186 (2019).
2. Park, S. H. et al. High areal capacity battery electrodes enabled by segregated nanotube networks. *Nat. Energy* **4**, 560–567 (2019).
3. Xiao, J. et al. Assessing cathode–electrolyte interphases in batteries. *Nat. Energy* **9**, 1463–1473 (2024).

4. Radin, M. D. et al. Narrowing the gap between theoretical and practical capacities in Li-ion layered oxide cathode materials. *Adv. Energy Mater.* **7**, 1602888 (2017).
5. Whittingham, M. S. Lithium batteries and cathode materials. *Chem. Rev.* **104**, 4271–4301 (2004).
6. Wen, B. et al. Ultrafast ion transport at a cathode–electrolyte interface and its strong dependence on salt solvation. *Nat. Energy* **5**, 578–586 (2020).
7. Liu, W. et al. Inhibition of transition metals dissolution in cobalt-free cathode with ultrathin robust interphase in concentrated electrolyte. *Nat. Commun.* **11**, 3629 (2020).
8. Yan, P. et al. Tailoring grain boundary structures and chemistry of Ni-rich layered cathodes for enhanced cycle stability of lithium-ion batteries. *Nat. Energy* **3**, 600–605 (2018).
9. Xu, J. et al. Electrolyte design for Li-ion batteries under extreme operating conditions. *Nature* **614**, 694–700 (2023).
10. Fang, M. et al. An Electrolyte with Less Space-Occupying Diluent at Cathode Inner Helmholtz Plane for Stable 4.6 V Lithium-Ion Batteries. *Angew. Chemie Int. Ed.* **63**, e202316839 (2024).
11. Wu, Y. et al. Performance and stability improvement of layered NCM lithium-ion batteries at high voltage by a microporous Al_2O_3 sol-gel coating. *ACS Omega* **4**, 13972–13980 (2019).
12. Liang, L. et al. High-entropy doping promising ultrahigh-Ni Co-free single-crystalline cathode toward commercializable high-energy lithium-ion batteries. *Sci. Adv.* **10**, 4472 (2024).
13. Wu, Y. et al. High-voltage and high-safety practical lithium batteries with ethylene carbonate-free electrolyte. *Adv. Energy Mater.* **11**, 2102299 (2021).
14. Zhao, W. et al. Extending the high-voltage operation of Graphite/NCM811 cells by constructing a robust electrode/electrolyte interphase layer. *Mater. Today Energy* **34**, 101301 (2023).
15. Shen, Y. et al. Sodium doping derived electromagnetic center of lithium layered oxide cathode materials with enhanced lithium storage. *Nano Energy* **94**, 106900 (2022).
16. Chen, H. et al. Exploring chemical, mechanical, and electrical functionalities of binders for advanced energy-storage devices. *Chem. Rev.* **118**, 8936–8982 (2018).
17. Zhang, M. et al. Coupling of multiscale imaging analysis and computational modeling for understanding thick cathode degradation mechanisms. *Joule* **7**, 201–220 (2023).
18. Yao, W. et al. A 5 V-class cobalt-free battery cathode with high loading enabled by dry coating. *Energy Environ. Sci.* **16**, 1620–1630 (2023).
19. Liu, Y., Zhang, R., Wang, J. & Wang, Y. Current and future lithium-ion battery manufacturing. *iScience* **24**, 102332 (2021).
20. Schumm, B. et al. Dry battery electrode technology: from early concepts to industrial applications. *Adv. Energy Mater.* **15**, 2406011 (2025).
21. Mun, J., Song, T., Park, M. S. & Kim, J. H. Paving the way for next-generation all-solid-state batteries: dry electrode technology. *Adv. Mater.* https://doi.org/10.1002/ADMA.202506123 (2025).
22. Huang, Z. et al. Grain rotation and lattice deformation during photoinduced chemical reactions revealed by in situ X-ray nanodiffraction. *Nat. Mater.* **14**, 691–695 (2015).
23. Ulvestad, U. et al. Topological defect dynamics in operando battery nanoparticles. *Science* **348**, 1344–1347 (2015).
24. Xu, J. et al. Lithium ion battery electrode manufacturing model accounting for 3D realistic shapes of active material particles. *J. Power Sources* **554**, 232294 (2023).
25. Poulsen, H. F. et al. Applications of high-energy synchrotron radiation for structural studies of polycrystalline materials. *J. Synchrotron Radiat.* **4**, 147–154 (1997).
26. Ulvestad, A. et al. Single particle nanomechanics in operando batteries via lensless strain mapping. *Nano Lett.* **14**, 5123–5127 (2014).
27. Zhang, X., Cui, Z. & Manthiram, A. Insights into the crossover effects in cells with high-nickel layered oxide cathodes and silicon/graphite composite anodes. *Adv. Energy Mater.* **12**, 2103611 (2022).
28. Pfeifer, M. A., Williams, G. J., Vartanyants, I. A., Harder, R. & Robinson, I. K. Three-dimensional mapping of a deformation field inside a nanocrystal. *Nature* **442**, 63–66 (2006).
29. Märker, K., Reeves, P. J., Xu, C., Griffith, K. J. & Grey, C. P. Evolution of structure and lithium dynamics in $LiNi_{0.8}Mn_{0.1}Co_{0.1}O_2$ (NMC811) cathodes during electrochemical cycling. *Chem. Mater.* **31**, 2545–2554 (2019).
30. Kondrakov, A. O. et al. Charge-transfer-induced lattice collapse in Ni-rich NCM cathode materials during delithiation. *J. Phys.Chem. C* **121**, 24381–24388 (2017).
31. Li, Y. et al. Elucidating the effect of borate additive in high-voltage electrolyte for Li-rich layered oxide materials. *Adv. Energy Mater.* **12**, 2103033 (2022).
32. Bauer, W., Nötzel, D., Wenzel, V. & Nirschl, H. Influence of dry mixing and distribution of conductive additives in cathodes for lithium ion batteries. *J. Power Sources* **288**, 359–367 (2015).
33. Tuinstra, F. & Koenig, J. L. Raman spectrum of graphite. *J. Chem. Phys.* **53**, 1126–1130 (1970).
34. Souza, P. C. T. et al. Martini 3: a general purpose force field for coarse-grained molecular dynamics. *Nat. Methods* **18**, 382–388 (2021).
35. Liu, Z. et al. FIB-SEM: emerging multimodal/multiscale characterization techniques for advanced battery development. *Chem. Rev.* https://doi.org/10.1021/ACS.CHEMREV.4C00831 (2025).
36. Koo, J. K. et al. Dry-processed ultra-high-energy cathodes (99.6wt%, 4.0 g cm^{-3}) using single-crystalline Ni-rich oxides. *Energy Storage Mater.* **78**, 104270 (2025).
37. Liu, Y. et al. Roll-to-roll solvent-free manufactured electrodes for fast-charging batteries. *Joule* **7**, 952–970 (2023).
38. Tan, D. H. S., Meng, Y. S. & Jang, J. Scaling up high-energy-density sulfidic solid-state batteries: A lab-to-pilot perspective. *Joule* **6**, 1755–1769 (2022).
39. Park, G. G., Park, Y. K., Park, J. K. & Lee, J. W. Flexible and wrinkle-free electrode fabricated with polyurethane binder for lithium-ion batteries. *RSC Adv.* **7**, 16244–16252 (2017).
40. Fang, C. et al. Pressure-tailored lithium deposition and dissolution in lithium metal batteries. *Nat. Energy* **6**, 987–994 (2021).
41. Fang, C. et al. Quantifying inactive lithium in lithium metal batteries. *Nature* **572**, 511–515 (2019).
42. Yang, Y. et al. Liquefied gas electrolytes for wide-temperature lithium metal batteries. *Energy Environ. Sci.* **13**, 2209–2219 (2020).
43. Qian, D., Xu, B., Chi, M. & Meng, Y. S. Uncovering the roles of oxygen vacancies in cation migration in lithium excess layered oxides. *Phys. Chem. Chem. Phys.* **16**, 14665–14668 (2014).
44. Park, N. R. et al. Understanding boron chemistry as the surface modification and electrolyte additive for Co-free lithium-rich layered oxide. *Adv. Energy Mater.* **14**, 2401968 (2024).
45. Li, W. et al. Enabling high areal capacity for Co-free high voltage spinel materials in next-generation Li-ion batteries. *J. Power Sources* **473**, 228579 (2020).
46. Zhang, M., Liu, H., Liu, Z., Fang, C. & Meng, Y. S. Modified coprecipitation synthesis of mesostructure-controlled Li-Rich layered oxides for minimizing voltage degradation. *ACS Appl. Energy Mater.* **1**, 3369–3376 (2018).
47. Thompson, A. P. et al. LAMMPS—a flexible simulation tool for particle-based materials modeling at the atomic, meso, and continuum scales. *Comput. Phys. Commun.* **271**, 108171 (2022).
48. Stukowski, A. Visualization and analysis of atomistic simulation data with OVITO–the Open Visualization Tool. *Model. Simul. Mater. Sci. Eng.* **18**, 015012 (2009).

49. Cooper, S. J., Bertei, A., Shearing, P. R., Kilner, J. A. & Brandon, N. P. TauFactor: an open-source application for calculating tortuosity factors from tomographic data. *SoftwareX* **5**, 203–210 (2016).
50. Llanos, P. S. et al. High voltage cycling stability of LiF-coated NMC811 electrode. *ACS Appl. Mater. Interfaces* **16**, 2216–2230 (2024).
51. Guo, Q. et al. The use of a single-crystal nickel-rich layered NCM cathode for excellent cycle performance of lithium-ion batteries. *New J. Chem.* **45**, 3652–3659 (2021).
52. Chang, B. et al. Highly elastic binder for improved cyclability of nickel-rich layered cathode materials in lithium-ion batteries. *Adv. Energy Mater.* **10**, 2001069 (2020).
53. Zhang, Y. et al. Improved performance of Li-metal|$LiNi_{0.8}Co_{0.1}Mn_{0.1}O_2$ Cells with high-loading cathodes and small amounts of electrolyte solutions containing fluorinated carbonates at 30 °C–55 °C. *J. Electrochem. Soc.* **167**, 070509 (2020).
54. Son, I. H. et al. Graphene balls for lithium rechargeable batteries with fast charging and high volumetric energy densities. *Nat. Commun.* **8**, 1561 (2017).
55. Kim, H.-J., Sim, H.-T., Oh, M.-K., Park, Y.-E. & Kim, D.-W. Effect of conductive carbon morphology on the cycling performance of dry-processed cathode with high mass loading for lithium-ion batteries. *J. Electrochem. Soc.* **171**, 100509 (2024).
56. Kremer, L. S. et al. Influence of the electrolyte salt concentration on the rate capability of ultra-thick NCM 622 electrodes. *Batter. Supercaps* **3**, 1172–1182 (2020).
57. Gao, Y. et al. Design lithium exchanged zeolite based multifunctional electrode additive for ultra-high loading electrode toward high energy density lithium metal battery. *Adv. Energy Mater.* **15**, 2403063 (2025).
58. Li, W. et al. Long-term cyclability of NCM-811 at high voltages in lithium-ion batteries: an in-depth diagnostic study. *Chem. Mater.* **32**, 7796–7804 (2020).
59. Jayawardana, C. et al. Lithium tetrafluoroborate-based ester electrolyte formulations to improve the operating temperature range in NCM 622 || graphite Li-ion batteries. *ACS Appl. Energy Mater.* **6**, 5300–5308 (2023).
60. Ivanishchev, A. V. et al. Li-ion diffusion characteristics of surface modified Ni-rich NCM cathode material. *J. Electroanal. Chem.* **932**, 117242 (2023).
61. Lee, S. et al. Efficient and scalable encapsulation process of highly conductive 1T-MoS2 nanosheets on Ni-rich LiNi0.83Co0.11Mn0.06O2 cathode materials for high-performance lithium-ion batteries. *Chem. Eng. J.* **470**, 144209 (2023).
62. Xin, F. et al. Enhanced long-term cycling life of Ni-rich NMC cathodes in high-voltage lithium–metal batteries. *ACS Appl. Mater. Interfaces* **16**, 50561–50566 (2024).
63. Sattar, T., Sim, S. J., Jin, B. S. & Kim, H. S. Dual function Li-reactive coating from residual lithium on Ni-rich NCM cathode material for lithium-ion batteries. *Sci. Rep.* **11**, 18590 (2021).
64. Kremer, L. S. et al. Manufacturing process for improved ultra-thick cathodes in high-energy lithium-ion batteries. *Energy Technol.* **8**, 1900167 (2020).

Acknowledgements

This work at UChicago was supported by the Energy Transition Network (ETN) at the Institute for Climate and Sustainable Growth (ICSG). The work performed at UCSD was supported by the Sustainable Power and Energy Center (SPEC). X.Z. and A.A.F. acknowledge the support of the BLESSED project funded by the European Union under Marie Sklodowska-Curie Actions (grant agreement no. 101072578). A.A.F. acknowledges the Institut Universitaire de France for the support. PFIB is supported by the funding and collaboration agreement between UCSD and Thermo Fisher Scientific on Advanced Characterization of Energy Materials (PFIB data collection and analysis). We acknowledge the use of facilities and instrumentation at the UC Irvine Materials Research Institute (IMRI), which is supported in part by the National Science Foundation through the UC Irvine Materials Research Science and Engineering Center (grant no. DMR-2011967). We thank B.-S. Lee and Z. Wu for the support of slurry processing. We acknowledge A. G. Shabalin, D. Cela, R. Basak, M. Wan, W. Cha and R. J. Harder for the help of operando single-particle XRD measurements. We also thank W. Hao and Y. Lin for the support of sample preparation and PFIB–SEM data collection. We also acknowledge L. Martinson for the help of Raman spectroscopy.

Author contributions

M.Z. and Y.S.M. conceived the ideas and designed the work. W.Y., N.T., N.R.P., R.J., G.R. and M.Z. fabricated thick electrode, performed electrochemical and mechanical performances testing. B.K.S., M.Z. and O.G.S. performed operando single-particle XRD measurements and analysis. X.Z. and A.A.F. designed and conducted the CGMD simulations with experimental inputs provided by M.Z. T.Y., H.G., C.-J.H. and Z.L. collected PFIB–SEM data. M.C. and M.Z. conducted the CBD connectivity analysis, tortuosity evaluation and the electronic current simulation. S.W. collected XPS data and analysis. M.Z. and S.W. performed Raman data analysis. W.Y. analysed powder XRD and ICP-MS data. M.Z. performed scanning transmission electron microscopy–EELS experiment and analysed the data. A.A.F., O.G.S. and Y.S.M. supervised the research. M.Z. wrote the paper. All authors contributed to the discussion and provided feedback on the paper.

Competing interests

The authors declare no competing interests.

Additional information

Supplementary information The online version contains supplementary material available at https://doi.org/10.1038/s41560-026-01981-3.

Correspondence and requests for materials should be addressed to Alejandro A. Franco, Oleg G. Shpyrko or Ying Shirley Meng.

Peer review information *Nature Energy* thanks Jong Hyeok Park and the other, anonymous, reviewer(s) for their contribution to the peer review of this work.

nature portfolio

Corresponding author(s): Ying Shirley Meng

Last updated by author(s): Dec 31, 2025

Reporting Summary

Nature Portfolio wishes to improve the reproducibility of the work that we publish. This form provides structure for consistency and transparency in reporting. For further information on Nature Portfolio policies, see our Editorial Policies and the Editorial Policy Checklist.

Statistics

For all statistical analyses, confirm that the following items are present in the figure legend, table legend, main text, or Methods section.

n/a	Confirmed
☒	☐ The exact sample size (*n*) for each experimental group/condition, given as a discrete number and unit of measurement
☒	☐ A statement on whether measurements were taken from distinct samples or whether the same sample was measured repeatedly
☒	☐ The statistical test(s) used AND whether they are one- or two-sided *Only common tests should be described solely by name; describe more complex techniques in the Methods section.*
☒	☐ A description of all covariates tested
☒	☐ A description of any assumptions or corrections, such as tests of normality and adjustment for multiple comparisons
☐	☒ A full description of the statistical parameters including central tendency (e.g. means) or other basic estimates (e.g. regression coefficient) AND variation (e.g. standard deviation) or associated estimates of uncertainty (e.g. confidence intervals)
☒	☐ For null hypothesis testing, the test statistic (e.g. *F*, *t*, *r*) with confidence intervals, effect sizes, degrees of freedom and *P* value noted *Give P values as exact values whenever suitable.*
☒	☐ For Bayesian analysis, information on the choice of priors and Markov chain Monte Carlo settings
☒	☐ For hierarchical and complex designs, identification of the appropriate level for tests and full reporting of outcomes
☒	☐ Estimates of effect sizes (e.g. Cohen's *d*, Pearson's *r*), indicating how they were calculated

Our web collection on statistics for biologists contains articles on many of the points above.

Software and code

Policy information about availability of computer code

Data collection	LAMMPS package
Data analysis	Avizo software with DualBeam 3D Wizard module 2024.1; Weka Trainable tool within Fiji (3.7.6); COMSOL Multiphysics 5.6; MATLAB R2020b; CasaXPS 2.3.25; Zview2

For manuscripts utilizing custom algorithms or software that are central to the research but not yet described in published literature, software must be made available to editors and reviewers. We strongly encourage code deposition in a community repository (e.g. GitHub). See the Nature Portfolio guidelines for submitting code & software for further information.

Data

Policy information about availability of data

All manuscripts must include a data availability statement. This statement should provide the following information, where applicable:

- Accession codes, unique identifiers, or web links for publicly available datasets
- A description of any restrictions on data availability
- For clinical datasets or third party data, please ensure that the statement adheres to our policy

All data generated or analysed during this study are included in the published Article and its Supplementary Information and Source Data files. Source data are provided with this paper.

Research involving human participants, their data, or biological material

Policy information about studies with human participants or human data. See also policy information about sex, gender (identity/presentation), and sexual orientation and race, ethnicity and racism.

Reporting on sex and gender	*Use the terms sex (biological attribute) and gender (shaped by social and cultural circumstances) carefully in order to avoid confusing both terms. Indicate if findings apply to only one sex or gender; describe whether sex and gender were considered in study design; whether sex and/or gender was determined based on self-reporting or assigned and methods used.* *Provide in the source data disaggregated sex and gender data, where this information has been collected, and if consent has been obtained for sharing of individual-level data; provide overall numbers in this Reporting Summary. Please state if this information has not been collected.* *Report sex- and gender-based analyses where performed, justify reasons for lack of sex- and gender-based analysis.*
Reporting on race, ethnicity, or other socially relevant groupings	*Please specify the socially constructed or socially relevant categorization variable(s) used in your manuscript and explain why they were used. Please note that such variables should not be used as proxies for other socially constructed/relevant variables (for example, race or ethnicity should not be used as a proxy for socioeconomic status).* *Provide clear definitions of the relevant terms used, how they were provided (by the participants/respondents, the researchers, or third parties), and the method(s) used to classify people into the different categories (e.g. self-report, census or administrative data, social media data, etc.)* *Please provide details about how you controlled for confounding variables in your analyses.*
Population characteristics	*Describe the covariate-relevant population characteristics of the human research participants (e.g. age, genotypic information, past and current diagnosis and treatment categories). If you filled out the behavioural & social sciences study design questions and have nothing to add here, write "See above."*
Recruitment	*Describe how participants were recruited. Outline any potential self-selection bias or other biases that may be present and how these are likely to impact results.*
Ethics oversight	*Identify the organization(s) that approved the study protocol.*

Note that full information on the approval of the study protocol must also be provided in the manuscript.

Field-specific reporting

Please select the one below that is the best fit for your research. If you are not sure, read the appropriate sections before making your selection.

☐ Life sciences ☐ Behavioural & social sciences ☐ Ecological, evolutionary & environmental sciences

For a reference copy of the document with all sections, see nature.com/documents/nr-reporting-summary-flat.pdf

Life sciences study design

All studies must disclose on these points even when the disclosure is negative.

Sample size	*Describe how sample size was determined, detailing any statistical methods used to predetermine sample size OR if no sample-size calculation was performed, describe how sample sizes were chosen and provide a rationale for why these sample sizes are sufficient.*
Data exclusions	*Describe any data exclusions. If no data were excluded from the analyses, state so OR if data were excluded, describe the exclusions and the rationale behind them, indicating whether exclusion criteria were pre-established.*
Replication	*Describe the measures taken to verify the reproducibility of the experimental findings. If all attempts at replication were successful, confirm this OR if there are any findings that were not replicated or cannot be reproduced, note this and describe why.*
Randomization	*Describe how samples/organisms/participants were allocated into experimental groups. If allocation was not random, describe how covariates were controlled OR if this is not relevant to your study, explain why.*
Blinding	*Describe whether the investigators were blinded to group allocation during data collection and/or analysis. If blinding was not possible, describe why OR explain why blinding was not relevant to your study.*

Behavioural & social sciences study design

All studies must disclose on these points even when the disclosure is negative.

Study description	*Briefly describe the study type including whether data are quantitative, qualitative, or mixed-methods (e.g. qualitative cross-sectional, quantitative experimental, mixed-methods case study).*
Research sample	*State the research sample (e.g. Harvard university undergraduates, villagers in rural India) and provide relevant demographic information (e.g. age, sex) and indicate whether the sample is representative. Provide a rationale for the study sample chosen. For studies involving existing datasets, please describe the dataset and source.*

Sampling strategy	*Describe the sampling procedure (e.g. random, snowball, stratified, convenience). Describe the statistical methods that were used to predetermine sample size OR if no sample-size calculation was performed, describe how sample sizes were chosen and provide a rationale for why these sample sizes are sufficient. For qualitative data, please indicate whether data saturation was considered, and what criteria were used to decide that no further sampling was needed.*
Data collection	*Provide details about the data collection procedure, including the instruments or devices used to record the data (e.g. pen and paper, computer, eye tracker, video or audio equipment) whether anyone was present besides the participant(s) and the researcher, and whether the researcher was blind to experimental condition and/or the study hypothesis during data collection.*
Timing	*Indicate the start and stop dates of data collection. If there is a gap between collection periods, state the dates for each sample cohort.*
Data exclusions	*If no data were excluded from the analyses, state so OR if data were excluded, provide the exact number of exclusions and the rationale behind them, indicating whether exclusion criteria were pre-established.*
Non-participation	*State how many participants dropped out/declined participation and the reason(s) given OR provide response rate OR state that no participants dropped out/declined participation.*
Randomization	*If participants were not allocated into experimental groups, state so OR describe how participants were allocated to groups, and if allocation was not random, describe how covariates were controlled.*

Ecological, evolutionary & environmental sciences study design

All studies must disclose on these points even when the disclosure is negative.

Study description	*Briefly describe the study. For quantitative data include treatment factors and interactions, design structure (e.g. factorial, nested, hierarchical), nature and number of experimental units and replicates.*
Research sample	*Describe the research sample (e.g. a group of tagged Passer domesticus, all Stenocereus thurberi within Organ Pipe Cactus National Monument), and provide a rationale for the sample choice. When relevant, describe the organism taxa, source, sex, age range and any manipulations. State what population the sample is meant to represent when applicable. For studies involving existing datasets, describe the data and its source.*
Sampling strategy	*Note the sampling procedure. Describe the statistical methods that were used to predetermine sample size OR if no sample-size calculation was performed, describe how sample sizes were chosen and provide a rationale for why these sample sizes are sufficient.*
Data collection	*Describe the data collection procedure, including who recorded the data and how.*
Timing and spatial scale	*Indicate the start and stop dates of data collection, noting the frequency and periodicity of sampling and providing a rationale for these choices. If there is a gap between collection periods, state the dates for each sample cohort. Specify the spatial scale from which the data are taken*
Data exclusions	*If no data were excluded from the analyses, state so OR if data were excluded, describe the exclusions and the rationale behind them, indicating whether exclusion criteria were pre-established.*
Reproducibility	*Describe the measures taken to verify the reproducibility of experimental findings. For each experiment, note whether any attempts to repeat the experiment failed OR state that all attempts to repeat the experiment were successful.*
Randomization	*Describe how samples/organisms/participants were allocated into groups. If allocation was not random, describe how covariates were controlled. If this is not relevant to your study, explain why.*
Blinding	*Describe the extent of blinding used during data acquisition and analysis. If blinding was not possible, describe why OR explain why blinding was not relevant to your study.*

Did the study involve field work? ☐ Yes ☐ No

Field work, collection and transport

Field conditions	*Describe the study conditions for field work, providing relevant parameters (e.g. temperature, rainfall).*
Location	*State the location of the sampling or experiment, providing relevant parameters (e.g. latitude and longitude, elevation, water depth).*
Access & import/export	*Describe the efforts you have made to access habitats and to collect and import/export your samples in a responsible manner and in compliance with local, national and international laws, noting any permits that were obtained (give the name of the issuing authority, the date of issue, and any identifying information).*
Disturbance	*Describe any disturbance caused by the study and how it was minimized.*

Reporting for specific materials, systems and methods

We require information from authors about some types of materials, experimental systems and methods used in many studies. Here, indicate whether each material, system or method listed is relevant to your study. If you are not sure if a list item applies to your research, read the appropriate section before selecting a response.

Materials & experimental systems

n/a	Involved in the study
☐	☐ Antibodies
☐	☐ Eukaryotic cell lines
☐	☐ Palaeontology and archaeology
☐	☐ Animals and other organisms
☐	☐ Clinical data
☐	☐ Dual use research of concern
☐	☐ Plants

Methods

n/a	Involved in the study
☐	☐ ChIP-seq
☐	☐ Flow cytometry
☐	☐ MRI-based neuroimaging

Antibodies

Antibodies used: *Describe all antibodies used in the study; as applicable, provide supplier name, catalog number, clone name, and lot number.*

Validation: *Describe the validation of each primary antibody for the species and application, noting any validation statements on the manufacturer's website, relevant citations, antibody profiles in online databases, or data provided in the manuscript.*

Eukaryotic cell lines

Policy information about cell lines and Sex and Gender in Research

Cell line source(s): *State the source of each cell line used and the sex of all primary cell lines and cells derived from human participants or vertebrate models.*

Authentication: *Describe the authentication procedures for each cell line used OR declare that none of the cell lines used were authenticated.*

Mycoplasma contamination: *Confirm that all cell lines tested negative for mycoplasma contamination OR describe the results of the testing for mycoplasma contamination OR declare that the cell lines were not tested for mycoplasma contamination.*

Commonly misidentified lines (See ICLAC register): *Name any commonly misidentified cell lines used in the study and provide a rationale for their use.*

Palaeontology and Archaeology

Specimen provenance: *Provide provenance information for specimens and describe permits that were obtained for the work (including the name of the issuing authority, the date of issue, and any identifying information). Permits should encompass collection and, where applicable, export.*

Specimen deposition: *Indicate where the specimens have been deposited to permit free access by other researchers.*

Dating methods: *If new dates are provided, describe how they were obtained (e.g. collection, storage, sample pretreatment and measurement), where they were obtained (i.e. lab name), the calibration program and the protocol for quality assurance OR state that no new dates are provided.*

☐ Tick this box to confirm that the raw and calibrated dates are available in the paper or in Supplementary Information.

Ethics oversight: *Identify the organization(s) that approved or provided guidance on the study protocol, OR state that no ethical approval or guidance was required and explain why not.*

Note that full information on the approval of the study protocol must also be provided in the manuscript.

Animals and other research organisms

Policy information about studies involving animals; ARRIVE guidelines recommended for reporting animal research, and Sex and Gender in Research

Laboratory animals: *For laboratory animals, report species, strain and age OR state that the study did not involve laboratory animals.*

Wild animals	*Provide details on animals observed in or captured in the field; report species and age where possible. Describe how animals were caught and transported and what happened to captive animals after the study (if killed, explain why and describe method; if released, say where and when) OR state that the study did not involve wild animals.*
Reporting on sex	*Indicate if findings apply to only one sex; describe whether sex was considered in study design, methods used for assigning sex. Provide data disaggregated for sex where this information has been collected in the source data as appropriate; provide overall numbers in this Reporting Summary. Please state if this information has not been collected. Report sex-based analyses where performed, justify reasons for lack of sex-based analysis.*
Field-collected samples	*For laboratory work with field-collected samples, describe all relevant parameters such as housing, maintenance, temperature, photoperiod and end-of-experiment protocol OR state that the study did not involve samples collected from the field.*
Ethics oversight	*Identify the organization(s) that approved or provided guidance on the study protocol, OR state that no ethical approval or guidance was required and explain why not.*

Note that full information on the approval of the study protocol must also be provided in the manuscript.

Clinical data

Policy information about clinical studies

All manuscripts should comply with the ICMJE guidelines for publication of clinical research and a completed CONSORT checklist must be included with all submissions.

Clinical trial registration	*Provide the trial registration number from ClinicalTrials.gov or an equivalent agency.*
Study protocol	*Note where the full trial protocol can be accessed OR if not available, explain why.*
Data collection	*Describe the settings and locales of data collection, noting the time periods of recruitment and data collection.*
Outcomes	*Describe how you pre-defined primary and secondary outcome measures and how you assessed these measures.*

Dual use research of concern

Policy information about dual use research of concern

Hazards

Could the accidental, deliberate or reckless misuse of agents or technologies generated in the work, or the application of information presented in the manuscript, pose a threat to:

No	Yes	
☐	☐	Public health
☐	☐	National security
☐	☐	Crops and/or livestock
☐	☐	Ecosystems
☐	☐	Any other significant area

Experiments of concern

Does the work involve any of these experiments of concern:

No	Yes	
☐	☐	Demonstrate how to render a vaccine ineffective
☐	☐	Confer resistance to therapeutically useful antibiotics or antiviral agents
☐	☐	Enhance the virulence of a pathogen or render a nonpathogen virulent
☐	☐	Increase transmissibility of a pathogen
☐	☐	Alter the host range of a pathogen
☐	☐	Enable evasion of diagnostic/detection modalities
☐	☐	Enable the weaponization of a biological agent or toxin
☐	☐	Any other potentially harmful combination of experiments and agents

Plants

Seed stocks — *Report on the source of all seed stocks or other plant material used. If applicable, state the seed stock centre and catalogue number. If plant specimens were collected from the field, describe the collection location, date and sampling procedures.*

Novel plant genotypes — *Describe the methods by which all novel plant genotypes were produced. This includes those generated by transgenic approaches, gene editing, chemical/radiation-based mutagenesis and hybridization. For transgenic lines, describe the transformation method, the number of independent lines analyzed and the generation upon which experiments were performed. For gene-edited lines, describe the editor used, the endogenous sequence targeted for editing, the targeting guide RNA sequence (if applicable) and how the editor was applied.*

Authentication — *Describe any authentication procedures for each seed stock used or novel genotype generated. Describe any experiments used to assess the effect of a mutation and, where applicable, how potential secondary effects (e.g. second site T-DNA insertions, mosiacism, off-target gene editing) were examined.*

ChIP-seq

Data deposition

☐ Confirm that both raw and final processed data have been deposited in a public database such as GEO.

☐ Confirm that you have deposited or provided access to graph files (e.g. BED files) for the called peaks.

Data access links
May remain private before publication. — *For "Initial submission" or "Revised version" documents, provide reviewer access links. For your "Final submission" document, provide a link to the deposited data.*

Files in database submission — *Provide a list of all files available in the database submission.*

Genome browser session
(e.g. UCSC) — *Provide a link to an anonymized genome browser session for "Initial submission" and "Revised version" documents only, to enable peer review. Write "no longer applicable" for "Final submission" documents.*

Methodology

Replicates — *Describe the experimental replicates, specifying number, type and replicate agreement.*

Sequencing depth — *Describe the sequencing depth for each experiment, providing the total number of reads, uniquely mapped reads, length of reads and whether they were paired- or single-end.*

Antibodies — *Describe the antibodies used for the ChIP-seq experiments; as applicable, provide supplier name, catalog number, clone name, and lot number.*

Peak calling parameters — *Specify the command line program and parameters used for read mapping and peak calling, including the ChIP, control and index files used.*

Data quality — *Describe the methods used to ensure data quality in full detail, including how many peaks are at FDR 5% and above 5-fold enrichment.*

Software — *Describe the software used to collect and analyze the ChIP-seq data. For custom code that has been deposited into a community repository, provide accession details.*

Flow Cytometry

Plots

Confirm that:

☐ The axis labels state the marker and fluorochrome used (e.g. CD4-FITC).

☐ The axis scales are clearly visible. Include numbers along axes only for bottom left plot of group (a 'group' is an analysis of identical markers).

☐ All plots are contour plots with outliers or pseudocolor plots.

☐ A numerical value for number of cells or percentage (with statistics) is provided.

Methodology

Sample preparation — *Describe the sample preparation, detailing the biological source of the cells and any tissue processing steps used.*

Instrument — *Identify the instrument used for data collection, specifying make and model number.*

Software — *Describe the software used to collect and analyze the flow cytometry data. For custom code that has been deposited into a community repository, provide accession details.*

Cell population abundance

Describe the abundance of the relevant cell populations within post-sort fractions, providing details on the purity of the samples and how it was determined.

Gating strategy

Describe the gating strategy used for all relevant experiments, specifying the preliminary FSC/SSC gates of the starting cell population, indicating where boundaries between "positive" and "negative" staining cell populations are defined.

☐ Tick this box to confirm that a figure exemplifying the gating strategy is provided in the Supplementary Information.

Magnetic resonance imaging

Experimental design

Design type

Indicate task or resting state; event-related or block design.

Design specifications

Specify the number of blocks, trials or experimental units per session and/or subject, and specify the length of each trial or block (if trials are blocked) and interval between trials.

Behavioral performance measures

State number and/or type of variables recorded (e.g. correct button press, response time) and what statistics were used to establish that the subjects were performing the task as expected (e.g. mean, range, and/or standard deviation across subjects).

Acquisition

Imaging type(s)

Specify: functional, structural, diffusion, perfusion.

Field strength

Specify in Tesla

Sequence & imaging parameters

Specify the pulse sequence type (gradient echo, spin echo, etc.), imaging type (EPI, spiral, etc.), field of view, matrix size, slice thickness, orientation and TE/TR/flip angle.

Area of acquisition

State whether a whole brain scan was used OR define the area of acquisition, describing how the region was determined.

Diffusion MRI ☐ Used ☐ Not used

Preprocessing

Preprocessing software

Provide detail on software version and revision number and on specific parameters (model/functions, brain extraction, segmentation, smoothing kernel size, etc.).

Normalization

If data were normalized/standardized, describe the approach(es): specify linear or non-linear and define image types used for transformation OR indicate that data were not normalized and explain rationale for lack of normalization.

Normalization template

Describe the template used for normalization/transformation, specifying subject space or group standardized space (e.g. original Talairach, MNI305, ICBM152) OR indicate that the data were not normalized.

Noise and artifact removal

Describe your procedure(s) for artifact and structured noise removal, specifying motion parameters, tissue signals and physiological signals (heart rate, respiration).

Volume censoring

Define your software and/or method and criteria for volume censoring, and state the extent of such censoring.

Statistical modeling & inference

Model type and settings

Specify type (mass univariate, multivariate, RSA, predictive, etc.) and describe essential details of the model at the first and second levels (e.g. fixed, random or mixed effects; drift or auto-correlation).

Effect(s) tested

Define precise effect in terms of the task or stimulus conditions instead of psychological concepts and indicate whether ANOVA or factorial designs were used.

Specify type of analysis: ☐ Whole brain ☐ ROI-based ☐ Both

Statistic type for inference

Specify voxel-wise or cluster-wise and report all relevant parameters for cluster-wise methods.

(See Eklund et al. 2016)

Correction

Describe the type of correction and how it is obtained for multiple comparisons (e.g. FWE, FDR, permutation or Monte Carlo).

Models & analysis

n/a	Involved in the study
☐	☐ Functional and/or effective connectivity
☐	☐ Graph analysis
☐	☐ Multivariate modeling or predictive analysis

Functional and/or effective connectivity

Report the measures of dependence used and the model details (e.g. Pearson correlation, partial correlation, mutual information).

Graph analysis

Report the dependent variable and connectivity measure, specifying weighted graph or binarized graph, subject- or group-level, and the global and/or node summaries used (e.g. clustering coefficient, efficiency, etc.).

Multivariate modeling and predictive analysis

Specify independent variables, features extraction and dimension reduction, model, training and evaluation metrics.